Modelling of Fission Chambers in Current Mode – Analytical Approach

Sébastien Chabod [1,a], Gabriele Fioni [2], Alain Letourneau [1], Frédéric Marie [1]

[1] *DSM/DAPNIA/SPhN, CEA-Saclay, 91191 Gif-Sur-Yvette, France*

[2] *DSM, CEA-Saclay, 91191 Gif-Sur-Yvette, France*

Abstract

A comprehensive theoretical model is proposed to explain the functioning of fission chambers operated in current mode, even in very high neutron fluxes. The calibration curves are calculated as a function of basic physical parameters as fission rate, gas pressure and geometry of the chambers. The output current at saturation is precisely calculated, as well as the maximum voltage to be applied in order to avoid avalanche phenomena. The electric field distortion due to the space charge phenomena is also estimated. Within this model, the characteristic responses of fission chambers are correctly reproduced, in agreement with the experience feedback obtained at the ILL/Grenoble High-Flux Reactor.

Key words: fission ionization chamber, current mode.
PACS: 29.40.Cs, 28.41.Rc

1. Introduction

Fission ionization chambers are widely used as neutron monitors in irradiating environments such as nuclear reactors, accelerators and medical facilities. They can be used in pulse mode, where each electronic pulse induced by a nuclear fission is counted event by event. Nevertheless, in high neutron fluxes (above 10^{14} n.cm^{-2}.s^{-1}), the pulse pile-up induced by the high fission rate requires a current mode acquisition, where each single event is not anymore individualised.

In order to carry out on-line measurements of transmutation rates of actinides at the Mini-Inca and Megapie installations [1-6], we have recently developed[b] sub-miniature cylindrical fission chambers designed to stand high temperatures and neutron fluxes up to several 10^{15} n.cm^{-2}.s^{-1}. Beside their use for nuclear waste transmutation studies, these detectors are useful tools for in-core neutron flux diagnostics of Generation-IV nuclear systems.

After several experiments in high neutron fluxes of about 10^{15} n.cm^{-2}.s^{-1}, we have observed that the responses of the chambers as a function of the applied voltage, namely the calibration curves, are perturbed. The shapes of the calibration curves differ significantly from those obtained during irradiation in neutron fluxes one order of magnitude lower. We have experimentally noticed that the pressure of the filling gas and the geometries of electrodes have a strong influence on the responses of the detectors, with differences that are accentuated in high-intensity neutron fluxes.

In order to have a clear understanding of the observed phenomena, we have developed an analytical model to study and predict the evolution of the calibration curves as a function of different physical parameters, as gas pressure, gas composition, applied voltage, during various conditions of irradiation, from low to high intensity neutron fluxes.

[a] E-mail: schabod@cea.fr, Phone: (33-1) 01 69 08 81 68, Fax: (33-1) 01 69 08 75 84
[b] in collaboration with CEA/DEN/SPEX Laboratory and PHOTONIS Company

This approach is described in the present paper. In the first part, the basic equations used to model the functioning of fission chambers in current mode are detailed. In a second part, this theoretical framework is applied to the calculation of the calibration curves.

2. Modelling of fission chambers

Cylindrical fission chambers are made of two coaxial electrodes (anode and cathode) separated by a filling gas, as shown in figure 5. The anode is usually coated with a fissile element. Under irradiation, neutrons induce fission reactions inside the deposit and high energy fission products (about 90 MeV/each on average for ^{235}U) are emitted in opposite directions. Thus, one is absorbed in the anode while the second crosses the inter-electrode space, ionizing the filling gas on its path and consequently generating a high number of electron-ion pairs. When a voltage is applied, an electric field is generated between the two electrodes, involving a migration of charges. The collected charges are responsible for the creation of an electric current. The layout of this current according to the voltage applied gives a characteristic curve, know as the calibration curve.

In the following, we will consider a standard cylindrical fission chamber with a 98.5 % pure ^{235}U deposit (as CFUT-C3[c] chambers used in the framework of the Mini-Inca and Megapie projects, see figure 5).

2. 1. Calculation of the charge pair density created by the fission products

In this section, we will evaluate the density N of electron-ion pairs created per unit of time by the fission products in the inter-electrode space. To simplify our calculations, we note N_{fst}, the number of fission products released per second and per unit of area at the anode. In cylindrical geometry, one can obtain

$$N_{fst} = \frac{\tau_f}{2\pi R_1 h}, \quad (2.1)$$

where h is the length of the deposit which partially covers the anode (see figure 1 for the notations). R_1 is the anode radius. τ_f is the fission rate, i.e. the number of fissions that take place inside the deposit per unit of time. Let us also note $X(d)$, the average number of pairs created by a fission product per unit of length travelled in the gas. X depends on the distance d covered by the fission product in the inter-electrode space. A first approximation consists in supposing that all the fission products leave the anode with a purely radial speed $\underline{v}$. In cylindrical coordinates, $\underline{v}$ can be written $v_r\,\underline{u}_r + v_\theta\,\underline{u}_\theta + v_z\,\underline{u}_z$. Consequently, this assumption fixes to zero the components v_θ and v_z. Within this simplified framework, one can obtain an expression for N that depends only on the r coordinate and that can be written

$$N(r) = \frac{N_{fst} R_1 X(r')}{r}, \quad (2.2)$$

with $r' = r - R_1$.

[c] CFUT-C3 chambers are manufactured by the PHOTONIS Company.

A second approach, developed by Poujade et Lebrun [7], consists in assuming that all fission products leave the deposit perpendicularly to the anode axis. The velocity component v_z is thus fixed to zero and the authors have shown that N depends once more only on r and can be written

$$N(r) = \int_{-\arccos\left(R_1/r\right)}^{\arccos\left(R_1/r\right)} \frac{N_{fst}}{\pi} X(r') \frac{R_1(r\cos(\theta) - R_1)}{r^2 + R_1^2 - 2rR_1\cos(\theta)} d\theta \,, \quad (2.3)$$

with $r' = \sqrt{R_1^2 + r^2 - 2rR_1\cos(\theta)}$.

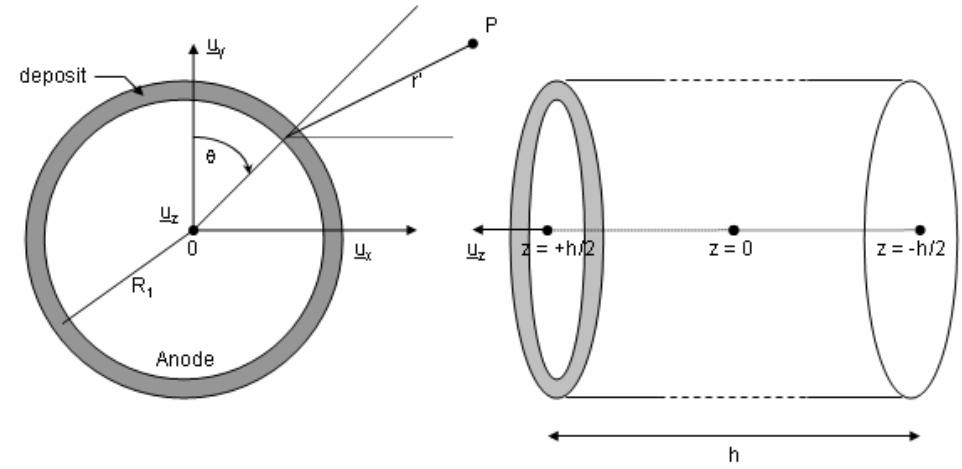

Fig. 1. Scheme of an anode and its deposit.

If the distance d covered by a fission product is small as compared to its mean free path, $X(d)$ remains about constant all along the trajectory. Thus we have $X(d) \approx X_0$. Within this framework, the (2.3) integral can be calculated and we have obtained the following expression

$$N(r) = \frac{2}{\pi} N_{fst} X_0 \arctan\left(\frac{R_1}{\sqrt{r^2 - R_1^2}}\right). \quad (2.4)$$

We can verify that

$$\begin{cases} N(r) \xrightarrow[r \to +\infty]{} \dfrac{2}{\pi} \dfrac{N_{fst} X_0 R_1}{r} \\ N(r) \xrightarrow[r \to R_1]{} N_{fst} X_0 \end{cases} . \quad (2.5)$$

The first two approaches started from approximations and led to simple expressions for $N(r)$. In order to calculate it precisely, let N_{ft} be the number of fission products ejected per second by an infinitesimal surface element dS of the anode. N_{ft} can be written in cylindrical coordinates

$$N_{ft} = N_{fst} R_1 \, dz' \, d\theta' \,, \quad (2.6)$$

where (R_1,θ',z') are the cylindrical coordinates of *dS*. The number of electron-ion pairs created per second, per surface element *dS*, in the infinitesimal volume $d\tau$ surrounding the point $P(r,\theta,z)$ in the gas is given by

$$d^2N = N_{ft}X(r')dr'\frac{d\Omega}{2\pi}, \quad (2.7)$$

where $d\Omega$ is the solid angle corresponding to the volume $d\tau$ seen from the element *dS*. r' is the distance between the point *P* and the element *dS*. In spherical coordinates, we can write

$$\begin{cases} d\tau = r'^2\sin(\varphi)dr'd\varphi d\psi \\ d\Omega = \sin(\varphi)d\varphi d\psi \end{cases}, \quad (2.8)$$

and d^2N thus becomes

$$d^2N = \frac{N_{ft}X(r')\sin(\varphi)dr'd\varphi d\psi}{2\pi}. \quad (2.9)$$

We obtain the density of pairs *dN* created around the point *P* by the element *dS* by dividing d^2N by $d\tau$

$$dN = \frac{d^2N}{d\tau} = \frac{N_{ft}X(r')}{2\pi r'^2} = \frac{N_{fst}R_1X(r')dz'd\theta'}{2\pi r'^2}. \quad (2.10)$$

In cylindrical coordinates, $r' = \sqrt{R_1^2 + r^2 - 2rR_1\cos(\theta'-\theta) + (z-z')^2}$ (2.11) and thus

$$dN(r,\theta,z) = \frac{N_{fst}R_1X(r')dz'd\theta'}{2\pi\left(R_1^2 + r^2 - 2rR_1\cos(\theta'-\theta) + (z-z')^2\right)}. \quad (2.12)$$

To obtain $N(r,z)$, the density of pairs created by the fission products per unit of time, we have only to integrate (2.12) expression over the surface of the anode,

$$\begin{aligned} N(r,z) &= \int_{\theta'=-\arccos(R_1/r)+\theta}^{\arccos(R_1/r)+\theta}\int_{z'=-h/2}^{h/2}\frac{N_{fst}R_1X(r')}{2\pi}\frac{dz'd\theta'}{\left(R_1^2 + r^2 - 2rR_1\cos(\theta'-\theta) + (z-z')^2\right)} \\ &= \int_{\theta'=-\arccos(R_1/r)}^{\arccos(R_1/r)}\int_{z'=-h/2}^{h/2}\frac{N_{fst}R_1X(r')}{2\pi}\frac{dz'd\theta'}{\left(R_1^2 + r^2 - 2rR_1\cos(\theta') + (z-z')^2\right)} \end{aligned}. \quad (2.13)$$

If we assume $X(r') \approx X_0$, we can get out the parameter *X* from the integral and write finally

$$N(r,z) = \frac{N_{fst}R_1X_0}{2\pi}F(r,z), \quad (2.14)$$

with $F(r,z) = \int_{\theta'=-\arccos(R_1/r)}^{\arccos(R_1/r)} \int_{z'=-h/2}^{h/2} \frac{dz'\,d\theta'}{\left(R_1^2 + r^2 - 2rR_1\cos(\theta') + (z-z')^2\right)}$. (2.15)

We have drawn on figures 2 and 3 the function F calculated for h = 1 cm and R_1 = 1.25 mm.

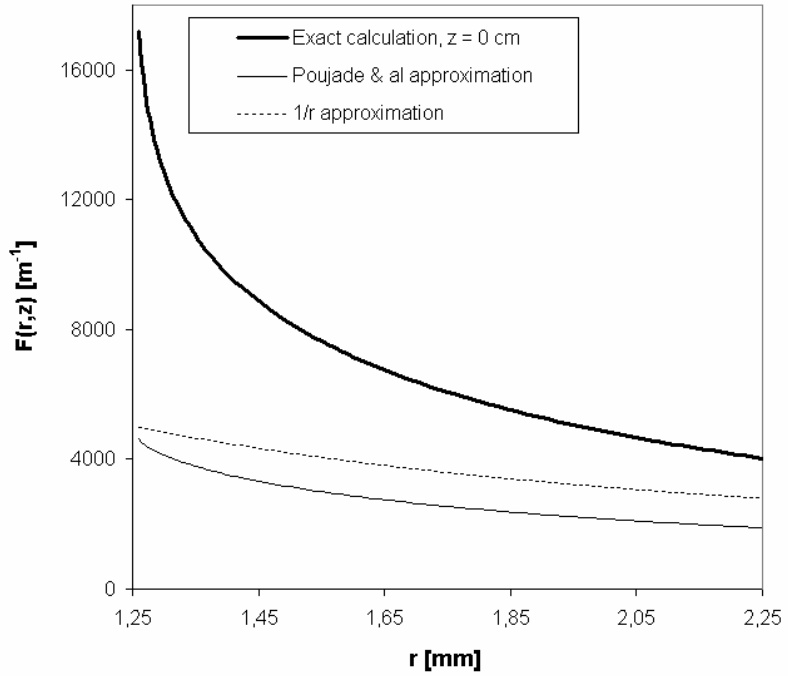

Fig. 2. Comparison between the exact formula of F, the $1/r$ approximation and the Poujade expression (R_1 = 1.25 mm, h = 1 cm).

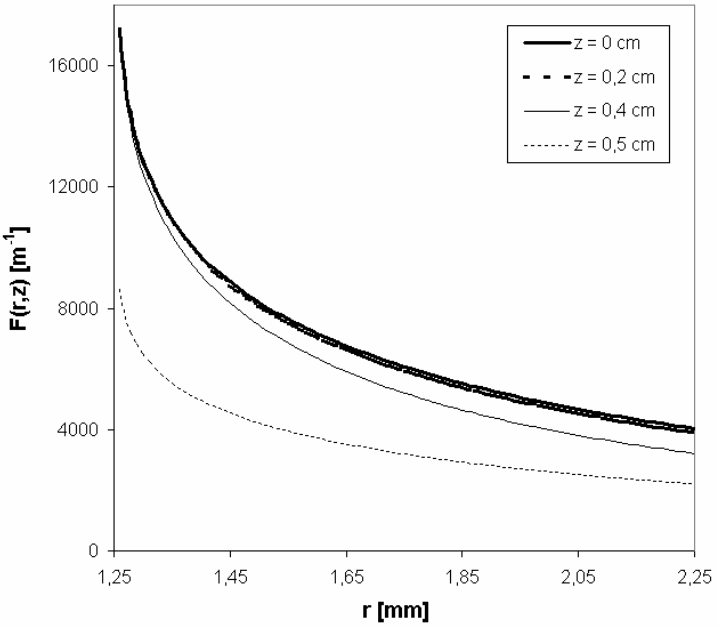

Fig. 3. Evolution of $F(r,z)$ with r inside the deposit zone for various z (R_1 = 1.25 mm, h = 1 cm).

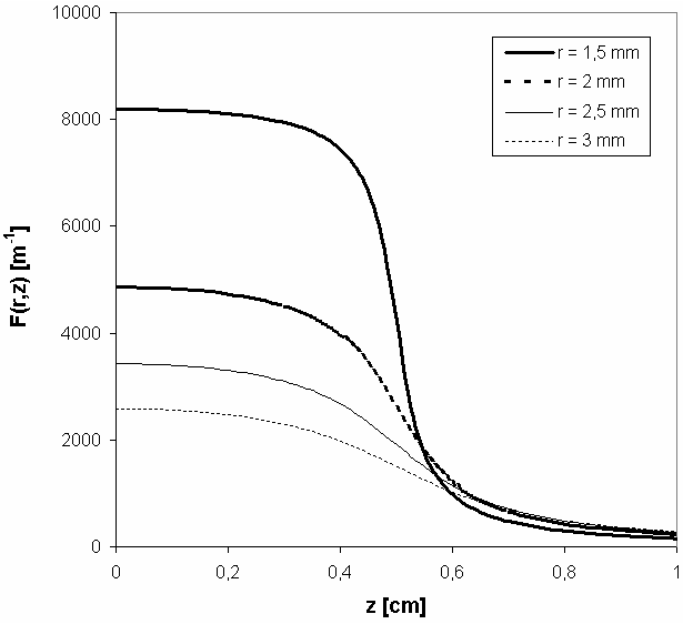

Fig. 4. Evolution of $F(r,z)$ with z for various r (R_1 = 1.25 mm, h = 1 cm).

We remark on figure 2 that the approximated expressions lead to a consequent undervaluation of the number of created pairs. On figures 3 and 4, we notice that $F(r,z)$ remains close to $F(r,0)$ in the deposit zone and falls brutally beyond. Consequently, we can modify the F expression to eliminate the z component

$$\langle F \rangle(r,z) = \begin{cases} F(r) = \dfrac{1}{h}\displaystyle\int_{z_{min}}^{z_{max}} F(r,z)dz & \text{inside the deposit zone (i.e. for - h/2} \le \text{z} \le \text{h/2)} \\ 0 & \text{outside the deposit zone (i.e. for z} \le \text{-h/2 and z} \ge \text{h/2)} \end{cases}, \quad (2.16)$$

where z_{min} and z_{max} are the limits in z of the inter-electrode space. Then, we assume that

$$N(r,z) = \begin{cases} N(r) = \dfrac{N_{fst} R_1 X_0}{2\pi} F(r) & \text{inside the deposit zone} \\ 0 & \text{outside the deposit zone} \end{cases}. \quad (2.17)$$

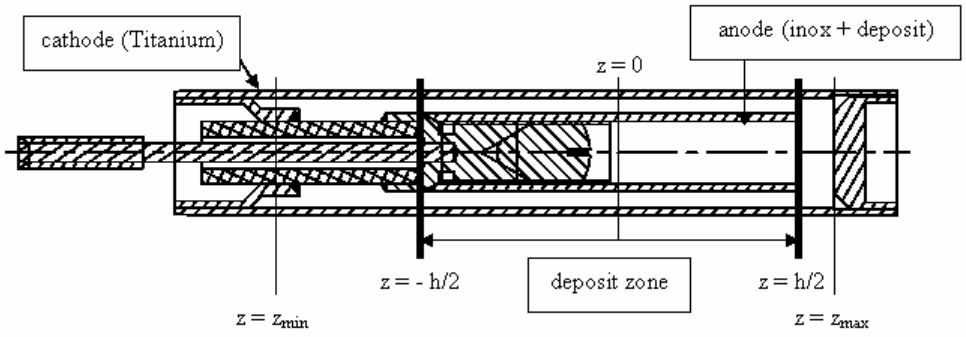

Fig. 5. Scheme of a CFUT-C3 class chamber.

For a CFUT-C3 chamber, z_{min} and z_{max} are respectively equal to -1.045 cm and 0.71 cm. We thus obtain the following evolutions of $\langle F \rangle(r,z)$ and $F(r)$, drawn on figures 6, 7 and 8.

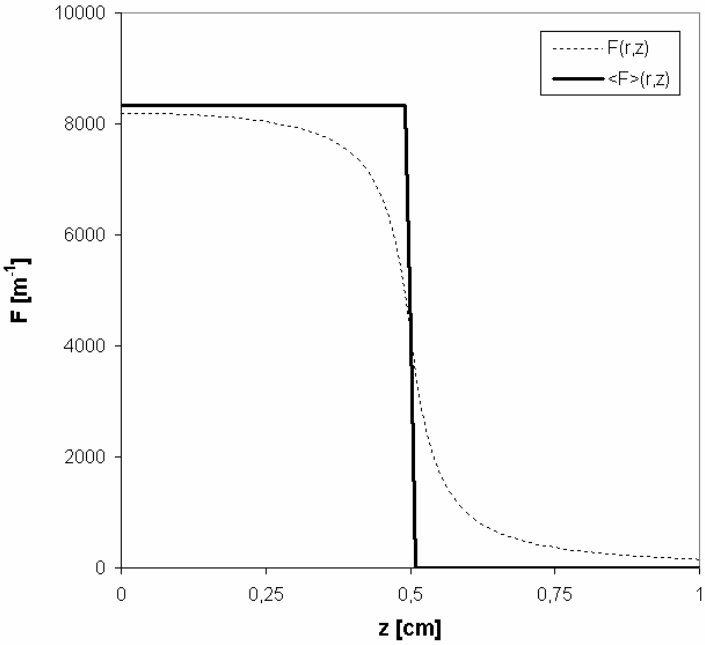

Fig. 6. Evolution of $F(r,z)$ and $\langle F \rangle(r,z)$ with z (R_1 = 1.25 mm, h = 1 cm).

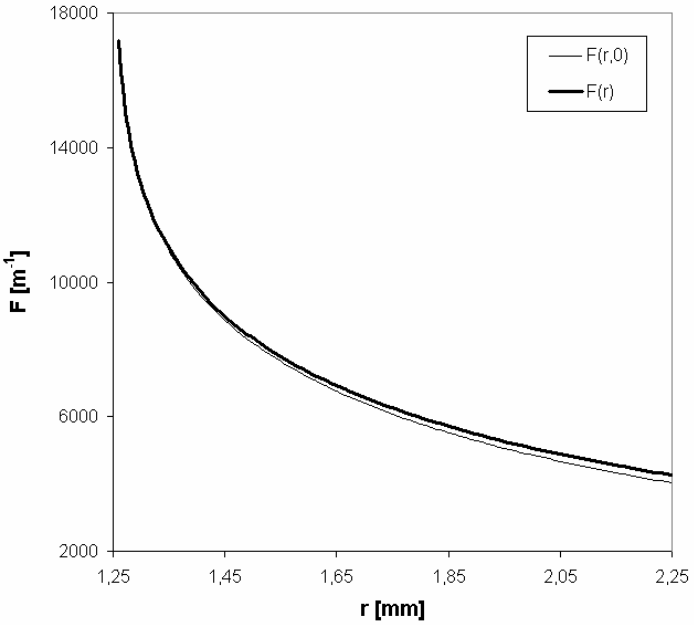

Fig. 7. Evolution of $F(r,0)$ and $F(r)$ with r (R_1 = 1.25 mm, h = 1 cm).

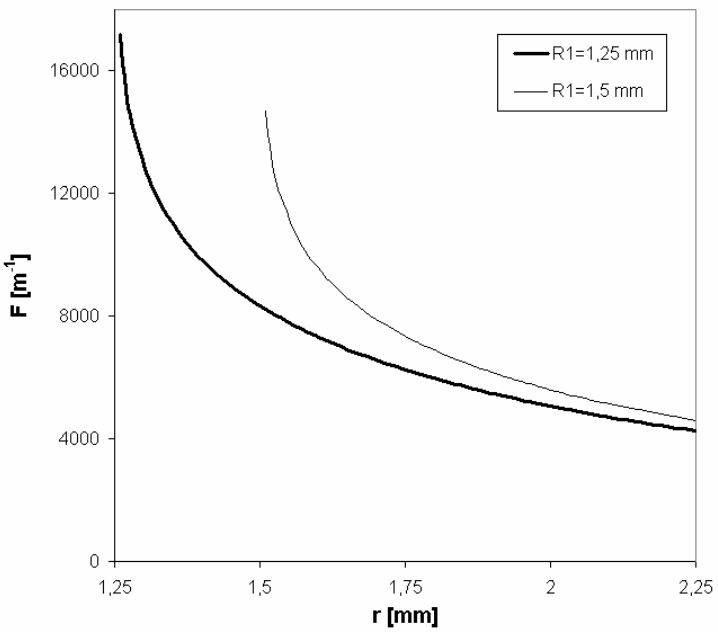

Fig. 8. Evolution of $F(r)$ with r for various R_1 radiuses (h = 1 cm).

We verify using (2.16) expression that

$$\int_{z_{\min}}^{z_{\max}} \langle F \rangle(r,z)dz = \int_{z_{\min}}^{z_{\max}} F(r,z)dz = hF(r)\,. \quad (2.18)$$

Thus, as it will be shown in section 3.1.2, the error induced by (2.17) approximation on the current at saturation is null.

2. 2. Coefficient X_0

The X_0 coefficient (see section 2.1) represents the number of electron-ion pairs created by a fission product per unit of length travelled in the inter-electrode space. Using SRIM software [8], we have calculated for Argon:

$$X_0 = 1.810^8 \times P_{[\text{bar}]} \text{ pairs.m}^{-1}, \quad (2.19)$$

when the chamber is filled at ambient temperature (T = 300 K). P is the gas pressure given in bar. This result is close to the value recommended by the ICRU report [9] which is worth $2.10^8 \times P_{[\text{bar}]}$ pairs.m^{-1}. The SRIM calculations have been conducted by averaging the loss energy in the gas over the complete distribution of ^{235}U fission products. We have also assumed that the average energy W necessary for a fission product to create a pair is 26.4 eV. In experiments, one can indeed find [9]

$$W = \begin{cases} 26.4\,\text{eV for } 5.3\,\text{MeV } \alpha \\ 26.66\,\text{eV for } 1.8\,\text{MeV protons} \\ 26.4 \pm 0.5\,\text{eV for electrons on average} \end{cases} . \quad (2.20)$$

Let us note now E_i the first ionization energy of the gas (15.75 eV for Argon), η the number of electrons produced and η_{ex} the number of excited Argon atoms (noted Ar^*) created by the fission products. One can obtain for the rare gases [9]

$$\begin{cases} W/E_i \approx 1{,}7 - 1{,}8 \\ \eta_{ex}/\eta \approx 0{,}4 - 0{,}5 \end{cases} . \quad (2.21)$$

We can notice that there is on average one excited atom for two electrons produced in Argon. In addition, Behle et al [10] give several threshold energies for some Ar + e^- reactions (table 1).

Reactions	**Threshold energy [eV]**
excitation	13,25
$Ar + e^- \rightarrow Ar^+ + 2e^-$	15,75
$Ar^+ + e^- \rightarrow Ar^{+*} + e^-$	19,22
$Ar^+ + e^- \rightarrow Ar^{2+} + 2e^-$	34,98

Tab. 1. Threshold energies for some Ar + e^- reactions.

To create Ar^{2+} ions, we remark that high energies are required. As a consequence, their number will be much lower than Ar^+ ions and we can neglect them.
Finally, the ICRU report [9] presents the evolution of the *W* coefficient of some gases after addition of several pollutants. In particular, the addition of Krypton, water or air in Argon involves a diminution of its *W* coefficient. For Helium at a pressure of one bar, the addition of 1 ‰ of Xenon, Argon, Krypton or CO_2 involves an increase in X_0 of a factor 1.4 to 1.5. A concentration of 0.00249 % of Argon in the same Helium induces a 4 eV reduction in its *W* coefficient, while a 0.0985 % Argon pollution is accompanied by a 15 eV fall of *W*. This non-negligible increase of the number of pairs created in presence of quantities, even small, of pollutants is a phenomenon known as the Jesse effect.

2. 3. Basic charge transport equations

The transport of electric charges inside the chamber obeys some basic equations. Let us note ρ_e and ρ_a, the electric densities respectively associated with electrons and Argon ions. Let us introduce also $\langle \underline{v}_e \rangle$ and $\langle \underline{v}_a \rangle$, the average drift velocities of electrons and ions. The charge conservation equations lead to the following system

$$\begin{cases} \dfrac{\partial n_e}{\partial t} + div\left(\rho_e \langle \underline{v}_e \rangle\right) = t^e_{SOURCE} + t^e_{LOSS} \\ \dfrac{\partial n_a}{\partial t} + div\left(\rho_a \langle \underline{v}_a \rangle\right) = t^a_{SOURCE} + t^a_{LOSS} \end{cases} . \quad (2.22)$$

The t_{SOURCE} and t_{LOSS} terms are the creation and disappearance terms. They represent the densities of electric charges which are created and destroyed per unit of time in gas. Their expressions will be detailed in the following sections.
In current mode, the chambers work in a stationary state. The temporal derivatives of (2.22) system thus vanish and it remains

$$\begin{cases} div\left(\rho_e \left\langle \underline{v}_e \right\rangle\right) = t^e_{SOURCE} + t^e_{LOSS} \\ div\left(\rho_a \left\langle \underline{v}_a \right\rangle\right) = t^a_{SOURCE} + t^a_{LOSS} \end{cases} . \quad (2.23)$$

In a cylindrical fission chamber, anode and cathode are two coaxial cylinders (see figure 5) of respective radiuses R_1 and R_2. We apply a voltage ΔV between anode and cathode. This difference of electric potential generates an electric field $\underline{E}$ that obeys Maxwell-Gauss equation and is written

$$\begin{cases} div(\underline{E}) = \dfrac{\rho_e + \rho_a}{\varepsilon_0} \\ \int \underline{E}.\underline{dl} = \Delta V \end{cases} . \quad (2.24)$$

In cylindrical geometry, if we suppose that the densities ρ_e and ρ_a depend only on the radial coordinate, noted r (see section 2.1), one can then write

$$\begin{cases} \underline{E} = E(r)\underline{u_r} \\ \dfrac{1}{r}\dfrac{\partial}{\partial r} rE(r) = \dfrac{\rho_e(r) + \rho_a(r)}{\varepsilon_0} \\ \int_{R_1}^{R_2} E(r)dr = \Delta V \end{cases} . \quad (2.25)$$

The electric field $\underline{E}$ is directed towards cathode. Consequently, ions migrate towards cathode while electrons move towards anode. As a consequence, we have

$$\begin{cases} \left\langle \underline{v}_e \right\rangle(r) = -\left\langle v_e \right\rangle(r)\, \underline{u}_r \\ \left\langle \underline{v}_a \right\rangle(r) = +\left\langle v_a \right\rangle(r)\, \underline{u}_r \end{cases} . \quad (2.26)$$

and we obtain the following system

$$\begin{cases} -\dfrac{1}{r}\dfrac{\partial}{\partial r} r\rho_e v_e = t^e_{SOURCE} - t^e_{LOSS} \\ \dfrac{1}{r}\dfrac{\partial}{\partial r} r\rho_a v_a = t^a_{SOURCE} - t^a_{LOSS} \end{cases} , \quad (2.27)$$

where v_e and v_a are respectively the average radial projections of the speed of electrons and Argon ions.

During this study, we will only consider Ar^+ ions (see section 2.2). The (2.27) system is thus reduced to 2 equations (instead of one equation for electrons and one per species of Ar^{n+} ions). Moreover, the absolute values of the creation and loss terms for electrons and Ar^+ ions become equal, the disappearance of a negative charge (one electron) involving the disappearance of a positive charge (one Ar^+ ion). Now, if we note

$$\begin{cases} \rho_e = -en_e \\ \rho_a = en_a \\ t^a_{SOURCE} = -t^e_{SOURCE} = eT_S \\ t^a_{LOSS} = -t^e_{LOSS} = eT_L \end{cases}, \quad (2.28)$$

the (2.27) system can be rewritten

$$\begin{cases} -\frac{1}{r}\frac{\partial}{\partial r} rn_e v_e = T_S - T_L \\ \frac{1}{r}\frac{\partial}{\partial r} rn_a v_a = T_S - T_L \end{cases}. \quad (2.29)$$

This system allows us to calculate the densities $n_e(r)$ and $n_a(r)$ of electrons and ions in gas. The T_S and T_L terms correspond here to the densities of electron-ion pairs respectively created and destroyed per unit of time in inter-electrode space.
The current I delivered by the chamber can be written

$$I = \iint_S (-en_e \underline{v}_e + en_a \underline{v}_a).\underline{dS} \,. \quad (2.30)$$

We can check that the current I is a constant of the (2.29) system. In cylindrical geometry, the (2.30) expression can be rewritten in the following way

$$I = 2\pi he(rn_e v_e + rn_a v_a) \,. \quad (2.31)$$

The electrodes are connected to an electric supply network. Thus, we have in stationary state

$$\begin{cases} n_e(r = R_2) = 0 \\ n_a(r = R_1) = 0 \end{cases}, \quad (2.32)$$

and expression (2.31) leads to

$$I = 2\pi heR_1 n_e(R_1) v_e(R_1) = 2\pi heR_2 n_a(R_2) v_a(R_2) \,. \quad (2.33)$$

To conclude this part, we simply note that the coupled resolution of the (2.25) and (2.29) systems give the functions $n_e(r)$, $n_a(r)$ and $E(r)$ according to the voltage applied to the electrodes. Thus, using (2.31) or (2.33) expressions, we are now able to calculate the current I as a function of the voltage ΔV, i.e. to draw the entire calibration curve.

2. 4. Creation and loss terms

The T_S and T_L terms appearing in system (2.29) are respectively called the source and loss terms. They represent the densities of charge pairs created or destroyed per unit of time inside the chamber.

2. 4. 1. Source terms

The T_S term is mainly the sum of two contributions. First, a term $T_S^{(1)}$ due to the ionization of the gas by the fission products. $T_S^{(1)}$ is equal to N and has been calculated in detail in section 2.1. Secondly, a term $T_S^{(2)}$ resulting from secondary ionizations due to electrons which have acquired enough kinetic energy in the electric field. The $T_S^{(2)}$ term is usually written

$$T_S^{(2)} = \alpha n_e v_e \text{ , (2.34)}$$

where α is the Townsend first ionization coefficient. When the variations of the electric field E are weak over an electron mean free path, α is only related to E and there are many theoretical or semi-empirical formulas which allow its calculation on limited intervals. We will retain in particular the Townsend formula

$$\frac{\alpha}{P} = Ae^{-\frac{BP}{E}} \text{ , (2.35)}$$

where P is the pressure of the filling gas. This formula is in rather good agreement with experimental results and has a physical justification. The coefficients A and B can indeed be calculated according to parameters like the mean free path l_0 of an electron in gas or the average fraction of energy lost by an electron during a collision with an atom (or a molecule) of gas. Zastawny [11] carried out a compilation of the values taken by A and B for many pure and mixed gases. Most of the semi-empirical expressions of α are proposed for low gas pressures. We have consequently used the BOLSIG software [12] to obtain estimates at atmospheric pressures (see figure 9).

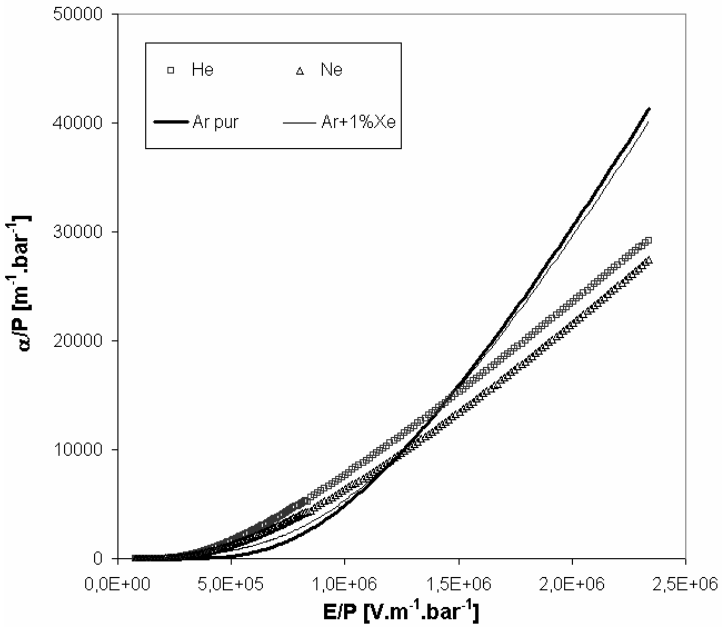

Fig. 9. Ratios of the ionization coefficient α over pressure P, calculated using BOLSIG software for various pure and mixed gases.

Lakshminarasimha et al [13] give also experimental values of α on a large range of E for several gases, in particular Argon.

2. 4. 2. Loss terms

The T_L term is mainly due to the recombination of electrons with ions. These processes of capture proceed in three steps, classified by size scale

- initial: the ejected electron recombines with the ion from which it comes from. Onsager [14] proposed a formula giving the fraction of pairs escaping from this initial recombination according to the electric field. This mode of recombination plays only at high pressures (10 to 100 atmospheres).
- columnar: the pairs can then recombine inside the ionized tracks left by the fission products in gas. These tracks have indeed high densities of charges.
- voluminal: the most general process. The electrons migrate in gas under the effect of the electric field and can recombine with any ion they meet.

For pressures close to the atmosphere, the dominating process is the voluminal recombination. The T_L term can thus be written as follows

$$T_L = k n_e n_a \text{ , (2.36)}$$

where k is generally called the "recombination coefficient". The estimation of the coefficient k is difficult and it exists only very few data. Langevin (1903) gives a theoretical expression of k

$$k_{th} = \frac{4\pi(\mu_e + \mu_a)e}{\varepsilon_0 \varepsilon_r} \approx \frac{4\pi\mu_e(E)e}{\varepsilon_0 \varepsilon_r} \text{ , (2.37)}$$

as μ_e (the mobility of electrons) is much higher than μ_a (the mobility of ions). This expression is valid when the mean free path l_0 is small in front of a characteristic distance a_0 given by

$$a_0 = \frac{e^2}{\varepsilon_r kT} \text{ , (2.38)}$$

where ε_r is equal to 1.00056 at a pressure of 0.1 MPa [15]. Shinsaka et al [16] have thereafter shown, for Argon at a temperature T of 300 K and a pressure P close to 100 bar, that

$$k_{\text{exp}} = 8.8 10^{-3} k_{th} \text{ . (2.39)}$$

By assuming that the coefficient k varies in $P^{1/2}$ [17], we have then a coarse estimate of k at lower pressures

$$k = 8.8 10^{-4} \sqrt{P}\, k_{th} \text{ . (2.40)}$$

For reduced electric fields E/P higher than 2.0 10^5 V.m^{-1}.bar^{-1}, μ_e is about 3. 10^{-2} m^2.V^{-1}.s^{-1} at a pressure of one bar (see section 2.7.1). We have thus a first estimate of k at one bar: $k \approx 5.6$ 10^{-12} m^3.s^{-1}.

Biondi [18] measures also $k \approx 8.8$ 10^{-13} m^3.s^{-1} at $P = 0.018$ bar and $T = 300$ K for Argon. For Neon, he obtained $k \approx 3.4$ 10^{-13} m^3.s^{-1} at $P = 0.03$ bar and $T = 300$ K. By applying the law in $P^{1/2}$, we obtain a second estimate of k at one bar: $k \approx 6.5$ 10^{-12} m^3/s. This result is close to the

value extrapolated from the results of Shinsaka [16]. For Neon, we obtain at one bar: $k \approx 2.10^{-12}$ $m^3.s^{-1}$.

2. 5. Discussion on the shape of a calibration curve

In cylindrical geometry, the current I obeys (2.31) equation. The densities n_e and n_a are given by the system (2.29) with the boundary conditions (2.32). Using the expressions of the creation and loss terms, we finally write

$$\begin{cases} -\frac{1}{r}\frac{\partial}{\partial r} r n_e v_e = N - k n_e n_a + \alpha n_e v_e \\ \frac{1}{r}\frac{\partial}{\partial r} r n_a v_a = N - k n_e n_a + \alpha n_e v_e \end{cases} . \quad (2.41)$$

This system can be integrated and we obtain

$$I = 2\pi e h \int_{R_1}^{R_2} r\left(N - k n_e n_a + \alpha n_e v_e\right) dr \; . \quad (2.42)$$

Equation (2.42) can be dissociated in three contributions

$$\begin{aligned} I &= I_1 + I_2 + I_3 \\ I_1 &= 2\pi e h \int_{R_1}^{R_2} r N(r) dr \\ I_2 &= -2\pi e h k \int_{R_1}^{R_2} r n_e n_a dr \\ I_3 &= 2\pi e h \int_{R_1}^{R_2} \alpha\left(E(r)\right) r n_e v_e dr \end{aligned} \quad . \quad (2.43)$$

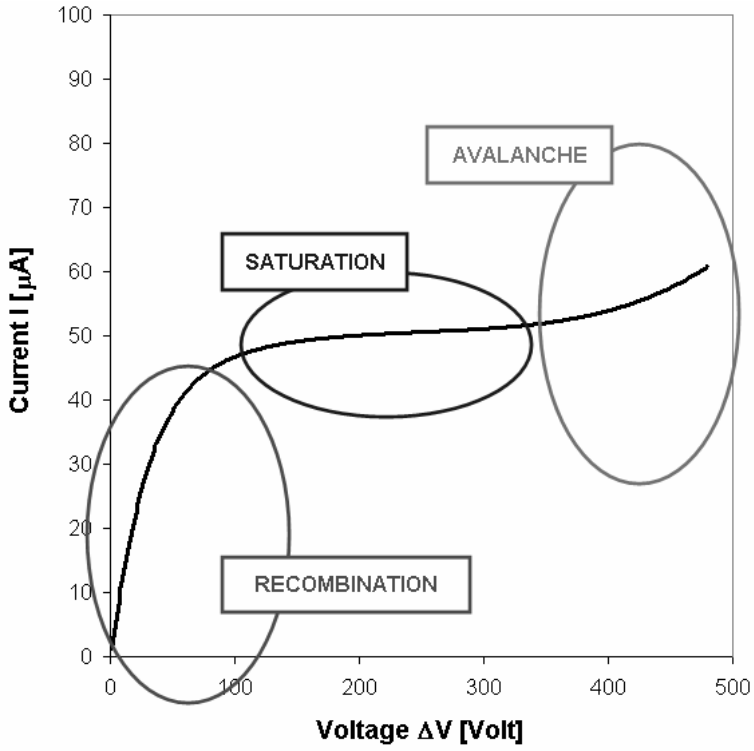

Fig. 10. Recombination, saturation and avalanche modes in a calibration curve.

The I_1 contribution is constant with the voltage ΔV applied and corresponds to the intensity delivered in a zone that we commonly call the "saturation plateau" (see figure 10).
Now, if one reduces the voltage applied at the electrodes, the electric field E will decrease and the charges will consequently circulate more and more slowly, accumulating in the filling gas. The densities n_e and n_a will thus increase and the recombination term I_2, which is negative, will take importance. As a consequence, the output current I will drop gradually below the saturation current I_1. This particular mode is called the "recombination mode" and we can indeed observe it at low voltages, on the left of the saturation zone (see figure 10).
In the same way, when the voltage increases, the electric field E is gradually reinforced. The first ionization coefficient $\alpha(E)$, up to now quasi zero, will increase slowly, until reaching a threshold ($E \approx 5.\ 10^5$ V.m^{-1} for Argon at one bar) where its growth accelerates brutally (see figure 9). Consequently, the I_3 contribution and the total current I will increase quickly. This fast increase is called the "avalanche mode" and frames on the right the saturation zone on a calibration curve (see figure 10).
A calibration curve thus results from a compromise between three modes, recombination, saturation and avalanche, whose key parameters will be studied in detail in this article.

2. 6. Space charges and distortion of the electric field

The equations which control the electric field inside a cylindrical chamber are written

$$\begin{cases} \frac{1}{r}\frac{\partial}{\partial r} rE(r) = \frac{e}{\varepsilon_0}\left(n_a(r) - n_e(r)\right) \\ \int_{R_1}^{R_2} E(r)dr = \Delta V \end{cases} . \quad (2.44)$$

The first equation can be easily integrated and we obtain

$$E = \frac{A}{r} + \frac{e}{r\varepsilon_0}\int_{R_1}^{r} r(n_a - n_e)dr \text{ . (2.45)}$$

We can demonstrate then that

$$\begin{aligned} A &= \frac{\Delta V}{\ln\left(\frac{R_2}{R_1}\right)} - \frac{e}{\varepsilon_0 \ln\left(\frac{R_2}{R_1}\right)}\int_{R_1}^{R_2} r \ln\left(\frac{R_2}{r}\right)(n_a - n_e)dr \\ &= R_1 E(R_1) \end{aligned} \text{ . (2.46)}$$

In absence of electric charges, we note that $A = \frac{\Delta V}{\ln\left(\frac{R_2}{R_1}\right)}$, (2.47)

and we find the usual unperturbed expression of the electric field

$$\underline{E} = \frac{\Delta V}{r \ln\left(\frac{R_2}{R_1}\right)}\underline{u}_r \text{ . (2.48)}$$

The presence of electric charges inside the chamber induces a distortion of the electric field, which does not vary any more as 1/*r*. We observe in particular, starting from equation (2.46), that an increase of the ion density n_a involves a reduction of the field at anode. The space charges phenomenon appears of crucial importance at high fission rates. We will have the opportunity to reconsider in detail this perturbation in the continuation of this study.

2. 7. Drift velocities of electrons and ions

The propagation of the electric charges in the filling gas is governed by the (2.29) system. Taking into account the diffusion processes, we can write

$$\begin{cases} -\frac{1}{r}\frac{\partial}{\partial r}\left(rn_e\mu_e E\right) - \frac{1}{r}\frac{\partial^2}{\partial r^2}\left(rn_e D_e\right) = T_S - T_L \\ \frac{1}{r}\frac{\partial}{\partial r}\left(rn_a\mu_a E\right) - \frac{1}{r}\frac{\partial^2}{\partial r^2}\left(rn_a D_a\right) = T_S - T_L \end{cases} \text{, (2.49)}$$

μ_e and μ_a are respectively the electronic and ionic mobilities. D_e and D_a are the radial diffusion coefficients of electrons and ions. These four parameters vary with the electric field, in particular for low values of *E*.

2. 7. 1. Electronic and ionic mobilities

The electronic mobility μ_e can be evaluated roughly using Lorentz formula

$$\mu_e \approx \frac{2}{3} e \left(\frac{2}{\pi m_e kT} \right)^{1/2} \frac{1}{n\sigma}, \quad (2.50)$$

where m_e is the electron mass, e the elementary electric charge, n the density of neutral gaseous atoms and σ the cross section of momentum transfer. For our calculations, we have however used BOLSIG simulations. The results are drawn on figures 11 and 12 and lead for Argon to the following adjustment

$$V_e(E) = \mu_e(E)E = 6.552610^{-18} \frac{E^3}{P^3} - 3.708810^{-10} \frac{E^2}{P^2} + 3.044310^{-2} \frac{E}{P} \quad . \quad (2.51)$$

The velocity V_e is given in m.s^{-1}, the electric field E in V.m^{-1} and the pressure P in bar.

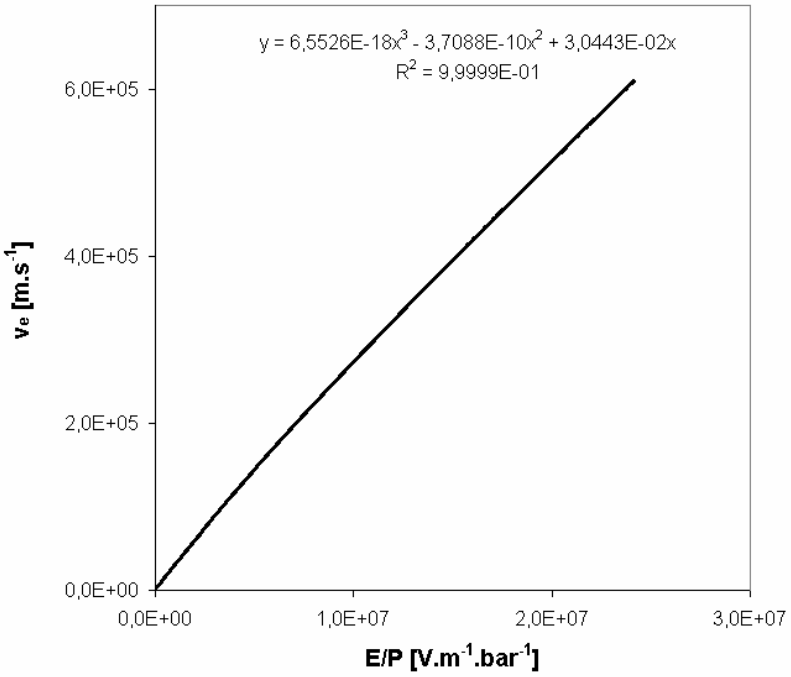

Fig. 11. Velocity V_e of electrons in Argon, calculated using BOLSIG software.

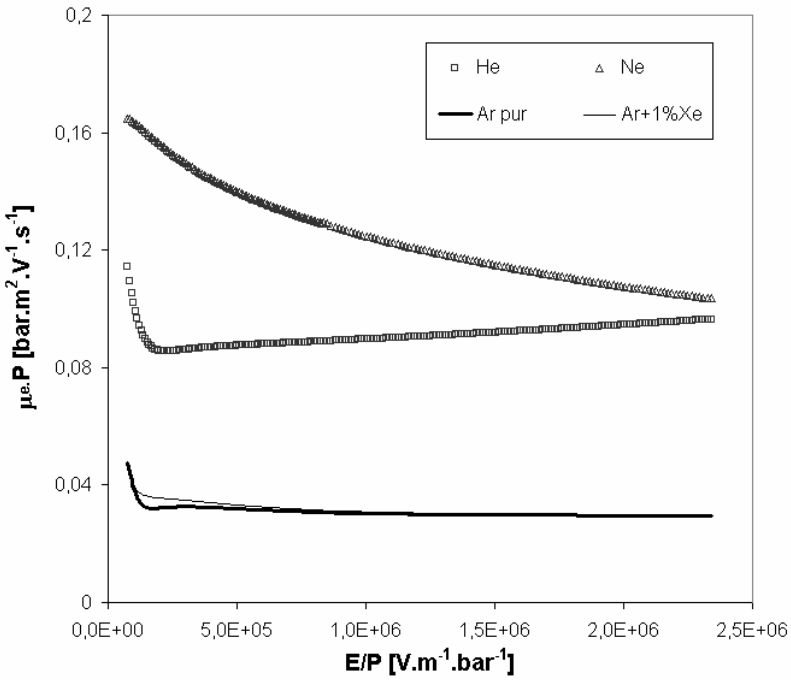

Fig. 12. Mobility of electrons in various pure and mixed gases, calculated using BOLSIG software.

Concerning the mobility μ_a of Ar^+ ions in Argon, experimental data [19] are presented on figure 13. The following formula is obtained

$$V_a(E) = \mu_a(E)E = 4.00491\,10^{92}\,\frac{E^5}{n^5} - 2.26951\,10^{75}\,\frac{E^4}{n^4} + 4.94461\,10^{57}\,\frac{E^3}{n^3} - 5.38091\,10^{39}\,\frac{E^2}{n^2} + 3.80691\,10^{21}\,\frac{E}{n} \quad , (2.52)$$

where V_a is given in $m.s^{-1}$. n is the density of Argon atoms. This adjustment is valid until $E/n = 2.\ 10^{-18}\ V.m^2$.

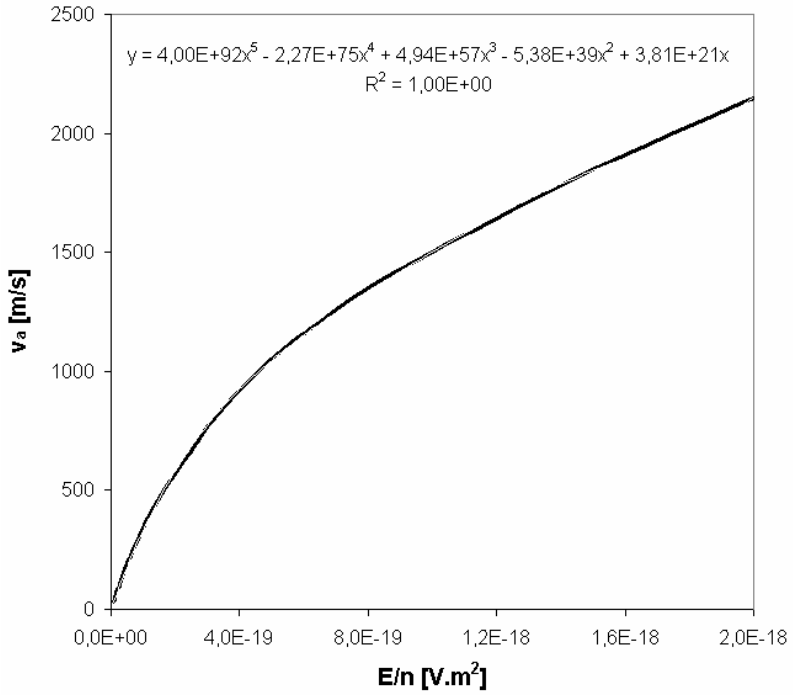

Fig. 13. Velocity V_a of Ar^+ ions in Argon.

Hornbeck [20] also proposes data for He^+, Ar^+ and Ne^+ ions in their respective gases.

2. 7. 2. Electronic and ionic diffusion

Lakshminarasimha et al [13] give several experimental values for the ratio $D_e^{\perp} / \mu_e$, where $D_e^{\perp}$ is the coefficient of diffusion perpendicular to the drift direction of electrons. They have shown that this ratio is about constant and is worth 7 Volt for *E*/*n* values lower than 1000 Td. The losses associated with this diffusion mode will not be taken into account in this study.
Concerning the diffusion of the charges in the direction of their drift, few experimental or theoretical data exist. Robertson et al [21] propose some values for the Argon ions, however they remain theoretical, D_a being too small to be measured accurately. Nevertheless, the coefficients D_e and D_a can be evaluated thanks to the Einstein formulas

$$\begin{cases} D_e = \dfrac{kT_e\mu_e}{e} \\ D_a = \dfrac{kT_a\mu_a}{e} \approx \dfrac{kT\mu_a}{e} \end{cases} . \quad (2.53)$$

Ions are heavy and collide frequently with the neutral atoms. Thus, it is commonly admitted that the ionic temperature T_a is constant, close to the temperature T of the gas. The electronic temperature T_e can be calculated using BOLSIG software (see figure 14). We obtain for example

$$\begin{cases} D_e \approx 0.2\ \mathrm{m}^2/\mathrm{s} \\ D_a \approx 5.10^{-6}\ \mathrm{m}^2/\mathrm{s} \end{cases}, \quad (2.54)$$

for Argon at a pressure of one bar, a temperature T of 300 K and an electric field E of 10^6 $V.m^{-1}$.

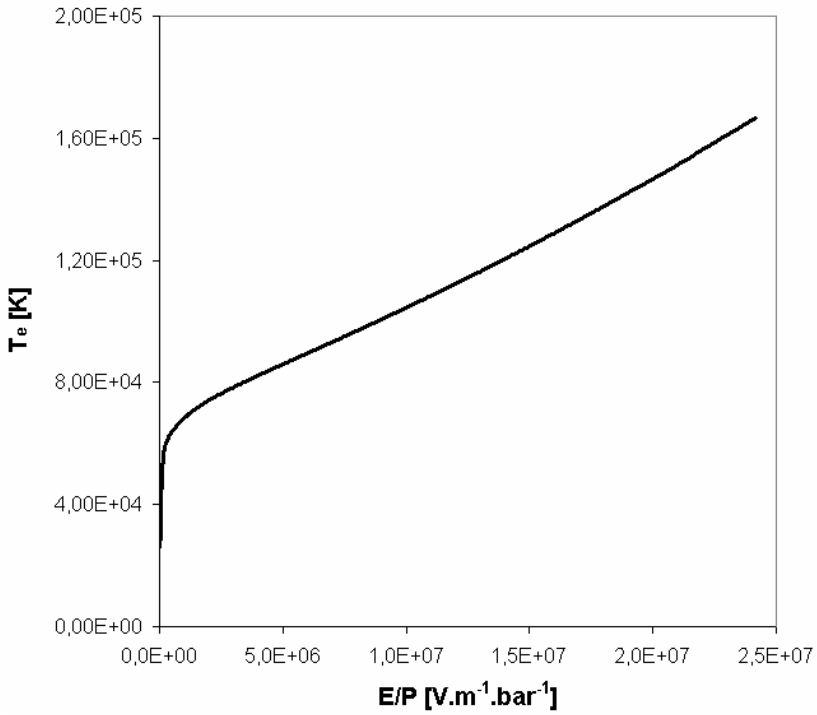

Fig. 14. Electronic temperature T_e in Argon as a function of the electric field E, calculated using BOLSIG software.

3. Application to sub-miniature cylindrical fission chambers

Figure 15 shows two experimental calibration curves obtained with a CFUT-C3 chamber at ILL for two neutron fluxes. At ordinary fission rates ($\leq 10^9$ f/s), the calibration curves present a saturation zone, where the current I delivered by the fission chamber varies little with the voltage ΔV applied to the electrodes. The I_{sat} current obtained at the saturation plateau is called the "saturation current". But, at high fission rates (higher than 5.10^9 f/s), we observe a deformation of the saturation plateau which ends to vanish completely. Consequently, the I_{sat} current can not be evaluated any more with accuracy.

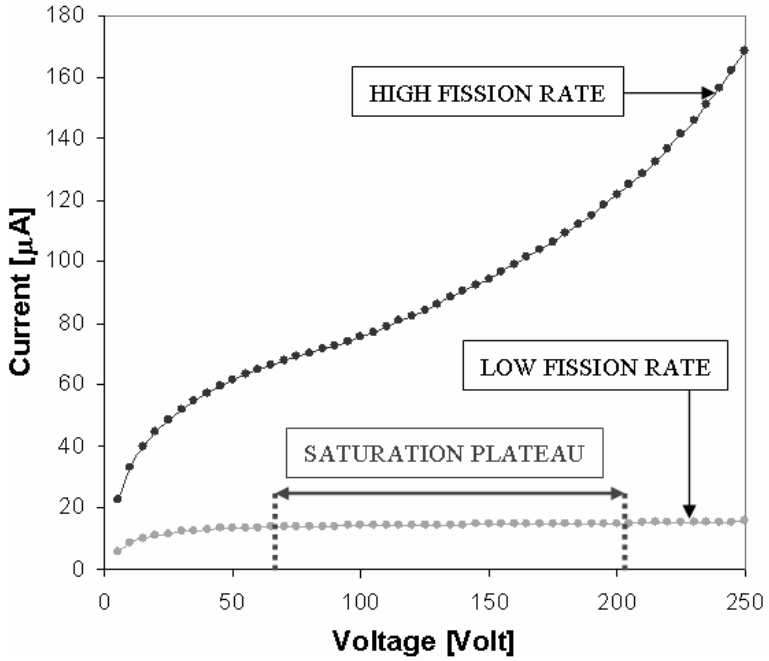

Fig. 15. Experimental calibration curves obtained with a CFUT-C3 fission chamber at ILL/Grenoble High-Flux Reactor. The saturation plateau is deformed at high fission rates and the corresponding saturation current can not be determined unambiguously.

In this section, we will gradually apply the theoretical framework described in the previous pages in order to calculate and to study the calibration curves of sub-miniature cylindrical fission chambers irradiated in neutron fluxes varying from low to high intensities.

3. 1. Current and charge densities at the saturation zone

At ordinary fission rates, the I_{sat} current is one of the crucial information delivered by a fission chamber operating in current mode. We will consequently present in this section the influence on the I_{sat} value of several parameters such as the length of the Uranium deposit or the radiuses of the electrodes.

3. 1. 1. Saturation current, $1/r$ approximation of $N(r)$ and associated error

At the saturation plateau, the recombination and avalanche terms are negligible[d]. We can thus write

$$\begin{cases} -\frac{1}{r}\frac{\partial}{\partial r} r n_e v_e = N(r) \\ \frac{1}{r}\frac{\partial}{\partial r} r n_a v_a = N(r) \end{cases} . \quad (3.1)$$

Expressions (2.17) and (2.42) then enable us to calculate the saturation current

$$I_{sat} = I_1 = 2\pi he \int_{R_1}^{R_2} r N(r) dr \, . \quad (3.2)$$

[d] In fact, the correct formulation would be rather that "the plateau exists because the recombination and avalanche processes are negligible".

If we approach $N(r)$ by the $1/r$ expression given by (2.2), we obtain

$$I_{sat} = 2\pi heX_0 R_1 N_{fst}(R_2 - R_1) = eX_0 \tau_f (R_2 - R_1)\,. \quad (3.3)$$

This common approximation induces directly an error on the saturation current that we want to estimate. We note ε, the error factor given by

$$\varepsilon = \frac{I_{sat} \text{ calculated for the } 1/r \text{ approximation of } N(r)}{I_{sat} \text{ calculated using exact expression of } N(r)}\,. \quad (3.4)$$

We can evaluate ε for various couples $\{R_1, R_2\}$ (see table 2).

	***R₂* [mm]**				
***R₁* [mm]**	1	1,25	1,5	1,75	2
1		0,43	0,48	0,52	0,55
1,25			0,41	0,47	0,51
1,5				0,4	0,46
1,75					0,39

Tab. 2. Values of ε for various $\{R_1,R_2\}$ couples. h = 1 cm.

We consequently notice that the error made on I_{sat} by the $1/r$ approximation is important (almost a factor 2) for fission chambers of millimetre sizes. It decreases gradually when the cathode radius R_2 increases.

3. 1. 2. Evolution of I_{sat} current with h, the deposit length

We want to estimate in this paragraph the impact on the saturation current of a modification of the deposit length h. Exceptionally, we will use for this study the exact expression of $N(r,z)$, the density of pairs created by the fission products per second. This density is given by the (2.14) equation. At saturation, the recombination and avalanche phenomena are secondary and all the primary charges created are collected. We can thus write

$$I_{sat} = e\iiint_{\Omega} rN(r,z)\,dr\,d\theta\,dz\,, \quad (3.5)$$

where Ω is the inter-electrode volume. Using (2.18) result, we consequently verify that the error on I_{sat} due to (2.17) approximation is null. Expression (3.5) can be rewritten in the following way

$$I_{sat} = \frac{X_0 \tau_f e}{2\pi} G(h, R_1, R_2, z_{\min}, z_{\max})\,, \quad (3.6)$$

with

$$G = \frac{1}{h}\int_{r=R_1}^{R_2}\int_{\phi=-\arccos(R_1/r)}^{\arccos(R_1/r)}\int_{z=z_{\min}}^{z_{\max}}\int_{z'=-h/2}^{h/2} \frac{r\,dz'\,dz\,d\phi\,dr}{R_1^2 + r^2 - 2rR_1\cos(\phi) + (z-z')^2}\,. \quad (3.7)$$

It can thus be broken up into two contributions: $I = I_1 + I_2$, given by

$$\begin{cases} I_1 = \dfrac{X_0 \tau_f e}{2\pi} G(h, R_1, R_2, -h/2, h/2) \\ I_2 = \dfrac{X_0 \tau_f e}{2\pi} \left(G(h, R_1, R_2, z_{\min}, -h/2) + G(h, R_1, R_2, h/2, z_{\max}) \right) \end{cases} . \quad (3.8)$$

The I_1 and I_2 contributions are respectively the currents created inside and outside the deposit zone. For a CFUT-C3 chamber, we have R_1 = 1.25 mm, R_2 = 1.75 mm, z_{min} = -1.045 cm and z_{max} = 0.71 cm. While varying h, we obtain the figures 16 and 17.

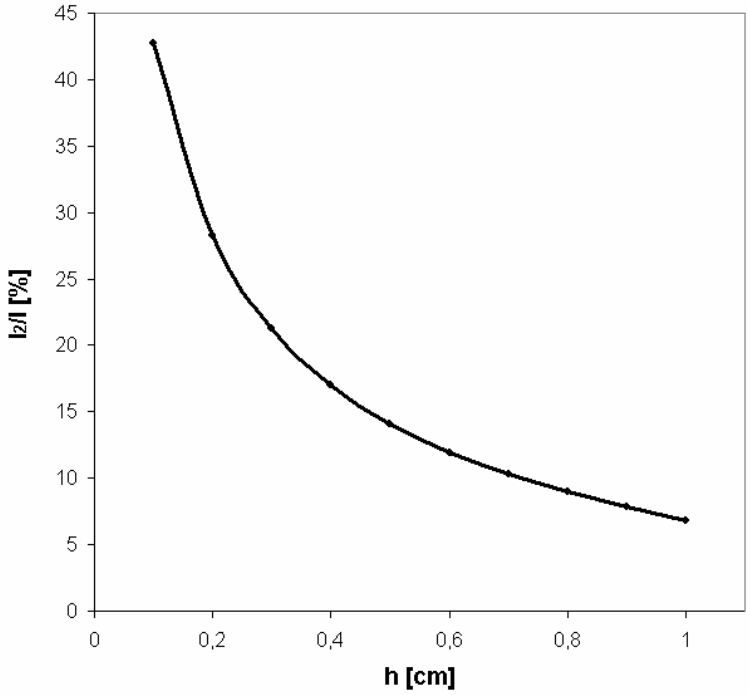

Fig. 16. Ratios in percentage of the I_2 current created outside the deposit zone over the total current I_{sat}, as a function of the deposit length h (z_{min} = -1.045 cm, z_{max} = 0.71 cm, R_1 = 1.25 mm, R_2 = 1.75 mm).

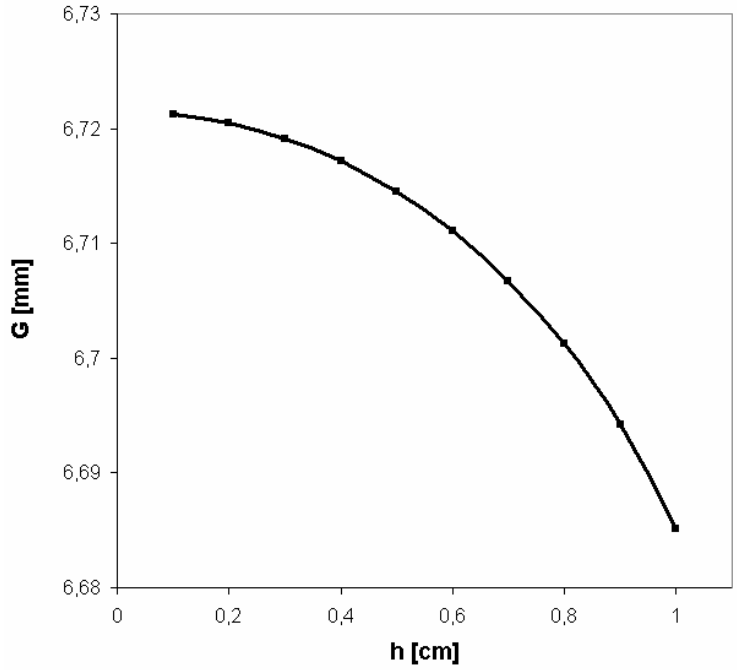

Fig. 17. Evolution of the factor G with the deposit length h (z_{min} = -1.045 cm, z_{max} = 0.71 cm, R_1 = 1.25 mm, R_2 = 1.75 mm).

First, we observe that the fraction of current created outside the deposit zone is weak for usual lengths h, close to 1 cm, as the I_2/I ratio is 6.8 %. Secondly, the total current delivered by the chamber varies very little with the size h of the deposit. Between h = 1 mm and h = 1 cm, the variation on I_{sat} is lower than 1 %.

3. 1. 3. Evolution of the saturation current with the radiuses of electrodes

Figures 18 to 21 present the evolution of the G factor, introduced in the previous paragraph and given by equation (3.7), as a function of the R_1 and R_2 radiuses of anode and cathode.

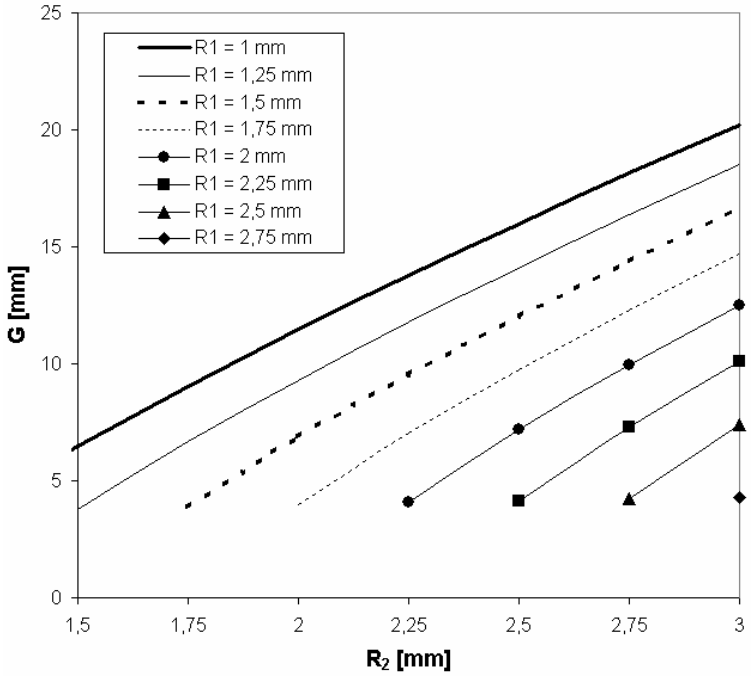

Fig. 18. Abacus of G values for various $\{R_1,R_2\}$ couples (h = 1 cm, z_{min} = -1.045 cm, z_{max} = 0.71 cm).

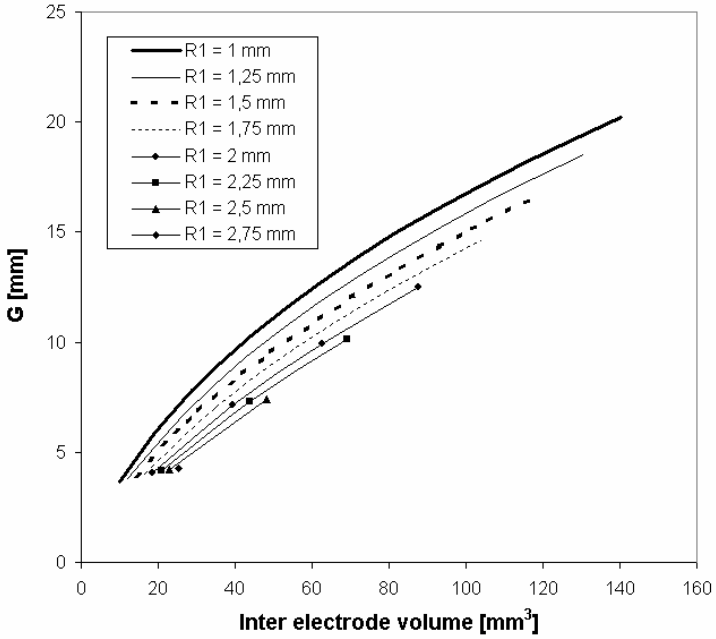

Fig. 19. Evolution of the factor G with the inter-electrode volume $V = (z_{max} - z_{min})(R_2^2 - R_1^2)$ (h = 1 cm, z_{min} = -1.045 cm, z_{max} = 0.71 cm).

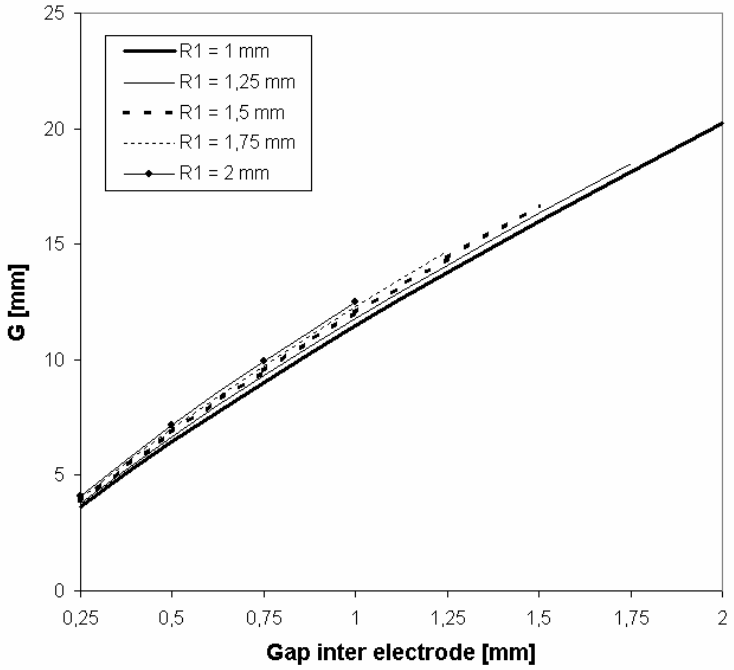

Fig. 20. Evolution of the factor G with the inter-electrode gap $d = (R_2 - R_1)$ (h = 1 cm, z_{min} = -1.045 cm, z_{max} = 0.71 cm).

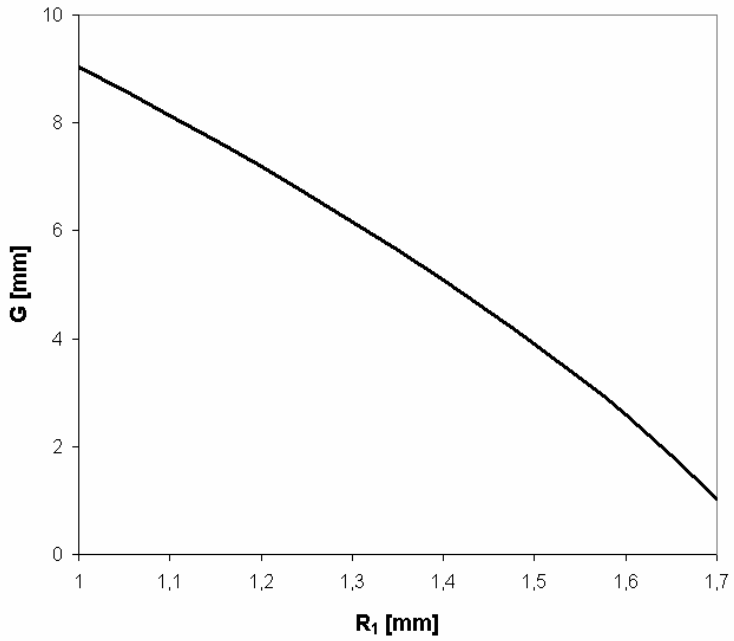

Fig. 21. Evolution of the factor G with the anode radius R_1 (R_2 = 1.75 mm, h = 1 cm, z_{min} = -1.045 cm, z_{max} = 0.71 cm).

We notice that, contrary to intuition, G is not proportional with the volume of the inter-electrode zone, which is proportional to (R_2^2 - R_1^2), but rather with the inter-electrode gap, i.e. with (R_2 - R_1).

3. 1. 4. Comparison between theoretical and experimental values of I_{sat}

For a standard CFUT-C3 class chamber, the factor G is 6.685 mm (see figure 18). Using the value X_0 = 1.8 $10^8 \times P_{[bar]}$ pairs.m^{-1} (see section 2.2), we have consequently

$$I_{sat} = \frac{X_0 \tau_f e}{2\pi} G = 3.068\,10^{-14}\ P_{[bar]} \times \tau_f \ . \quad (3.9)$$

During the past three years, we have irradiated at several occasions CFUT-C3 fission chambers in the High Flux Reactor (HFR) of Laue Langevin Institute (ILL) [1,6]. The Argon pressures inside the chambers ranged between 0.9 and 1.16 bar, the neutron fluxes between 6.10^{13} and 1.10^{15} n.cm^{-2}.s^{-1} and the ^{235}U deposit masses between 4 and 40 µg. The ratios of the calculated currents over the experimental ones are plotted on figure 22.

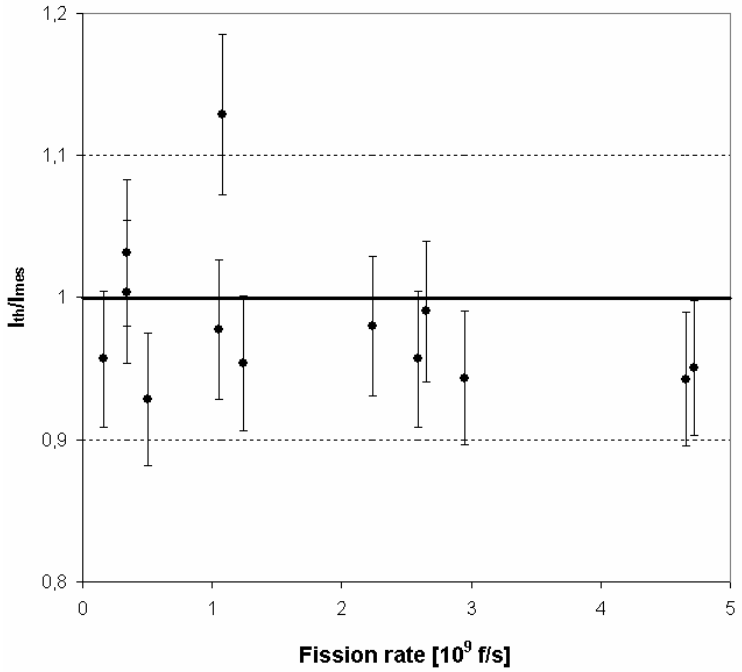

Fig. 22. Ratios of the theoretical currents over the experimental ones as a function of the fission rate. The experimental values have been obtained at the operating point of the calibration curves (see section 3.3.1).

We observe an overall good agreement between experimental data and theoretical calculations for fission rates lower than 5.10^9 f/s.

3. 2. Distortion of the electric field at saturation

In cylindrical geometry, the electric field obeys equation (2.45). In absence of electric charges, *E* is reduced to expression (2.48). As a consequence, we can rewrite *E* as the sum of two contributions

$$E = E_{\text{without charges}} + \delta E \text{ , (3.10)}$$

with

$$\begin{cases} E_{\text{without charges}} = \dfrac{\Delta V}{\ln\left(\dfrac{R_2}{R_1}\right)}\dfrac{1}{r} \\ \delta E = \dfrac{e}{\varepsilon_0 r}\int_{R_1}^{r} r(n_a - n_e)dr - \dfrac{e}{\varepsilon_0 \ln\left(\dfrac{R_2}{R_1}\right) r}\int_{R_1}^{R_2} r\ln\left(\dfrac{R_2}{r}\right)(n_a - n_e)dr \end{cases} \text{ . (3.11)}$$

We can estimate the densities n_e and n_a at saturation using (3.1) system

$$\begin{cases} r n_e v_e = \int_{r}^{R_2} rN(r)dr \\ r n_a v_a = \int_{R_1}^{r} rN(r)dr \end{cases} \text{ . (3.12)}$$

By re-injecting these expressions in (3.11) equations, we obtain

$$\frac{\delta E}{E_{\text{without charges}}} = \frac{e}{\varepsilon_0 \Delta V}\left[\begin{array}{l}\int_{R_1}^{r} \ln\left(R_2 / R_1\right)\left(\frac{1}{v_a}\int_{R_1}^{r} rN(r)dr - \frac{1}{v_e}\int_{r}^{R_2} rN(r)dr\right)dr \\ \qquad -\int_{R_1}^{R_2} \ln\left(R_2 / r\right)\left(\frac{1}{v_a}\int_{R_1}^{r} rN(r)dr - \frac{1}{v_e}\int_{r}^{R_2} rN(r)dr\right)dr\end{array}\right]. \quad (3.13)$$

At the first order, when the perturbations due to the space charges are not too important and by neglecting the diffusion processes, the electronic and ionic drift velocities are given by

$$\begin{cases} v_a \approx \mu_a(E_{\text{without charges}}) \times E_{\text{without charges}} \approx \mu_a(r)\dfrac{\Delta V}{\ln\left(\dfrac{R_2}{R_1}\right)r} \\ v_e \approx \mu_e(E_{\text{without charges}}) \times E_{\text{without charges}} \approx \mu_e(r)\dfrac{\Delta V}{\ln\left(\dfrac{R_2}{R_1}\right)r} \end{cases} . \quad (3.14)$$

In the following calculations, the μ_e and μ_a mobilities will obey (2.51) and (2.52) expressions. In addition, as (see equations (2.1) and (2.17))

$$N(r) = \frac{N_{fst} R_1 X_0}{2\pi} F(r) = \frac{\tau_f X_0}{4\pi^2 h} F(r), \quad (3.15)$$

we can note that $\frac{\delta E}{E} \propto \tau_f$. (3.16).

The higher the fission rate, the more the perturbations due to the space charges become important.

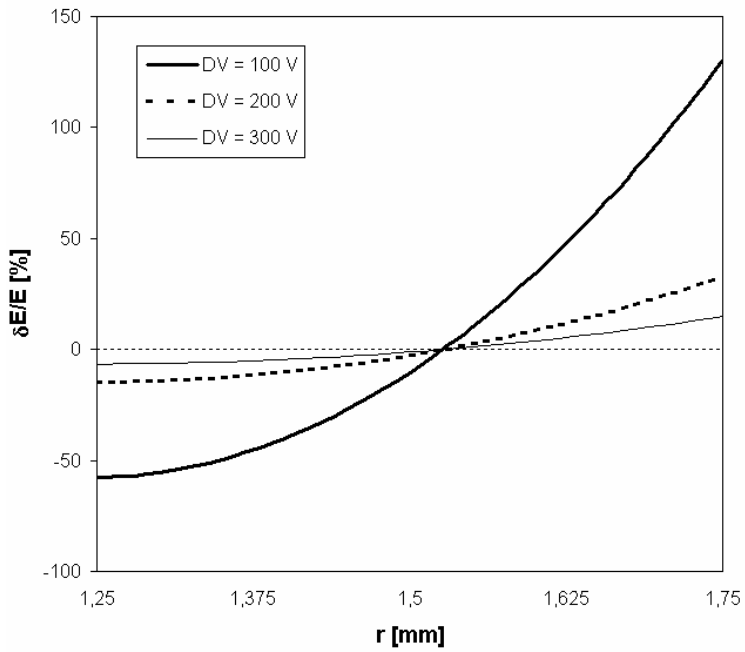

Fig. 23. Distortion of the electric field as a function of the radial distance r for several voltages ΔV (the filling gas is Argon at a pressure of 1 bar, R_1 = 1.25 mm, R_2 = 1.75 mm, h = 1 cm, $\tau_f = 10^9$ f/s).

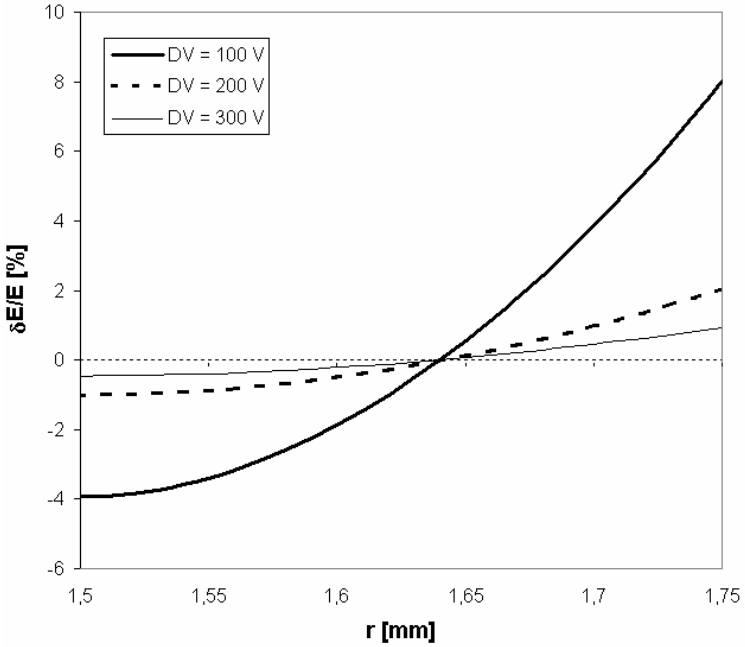

Fig. 24. Distortion of the electric field as a function of the radial distance r for several voltages ΔV (the filling gas is Argon at a pressure of 1 bar, R_1 = 1.5 mm, R_2 = 1.75 mm, h = 1 cm, $\tau_f = 10^9$ f/s).

We notice on figures 23 and 24 that the space charges induce a diminution of the electric field at anode and an increase at cathode. This field distortion effect is reinforced when the voltage decreases. Indeed, at low voltages, the electric charges move slowly. Consequently, their collection times increase and they accumulate in gas, perturbing the electric field.
We also observe that the distortion is maximal at cathode: $(\delta E/E)_{max} = (\delta E/E)$ $(r = R_2)$, and falls quickly when the inter-electrode gap decreases.

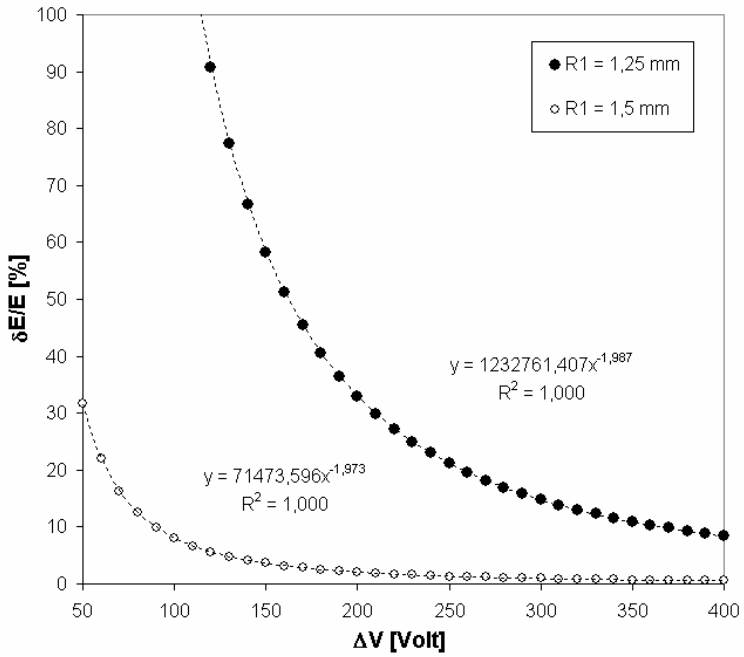

Fig. 25. Maximal distortion of the electric field as a function of the voltage ΔV (the filling gas is Argon at a pressure of 1 bar, R_2 = 1.75 mm, h = 1 cm, $\tau_f = 10^9$ f/s).

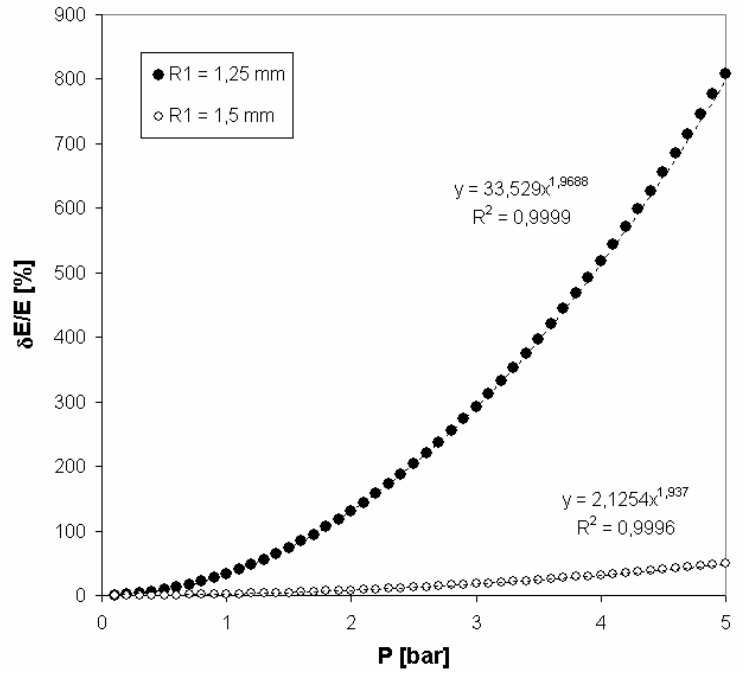

Fig. 26. Maximal distortion of the electric field as a function of pressure P (R_2 = 1.75 mm, h = 1 cm, ΔV = 200 V, $\tau_f = 10^9$ f/s).

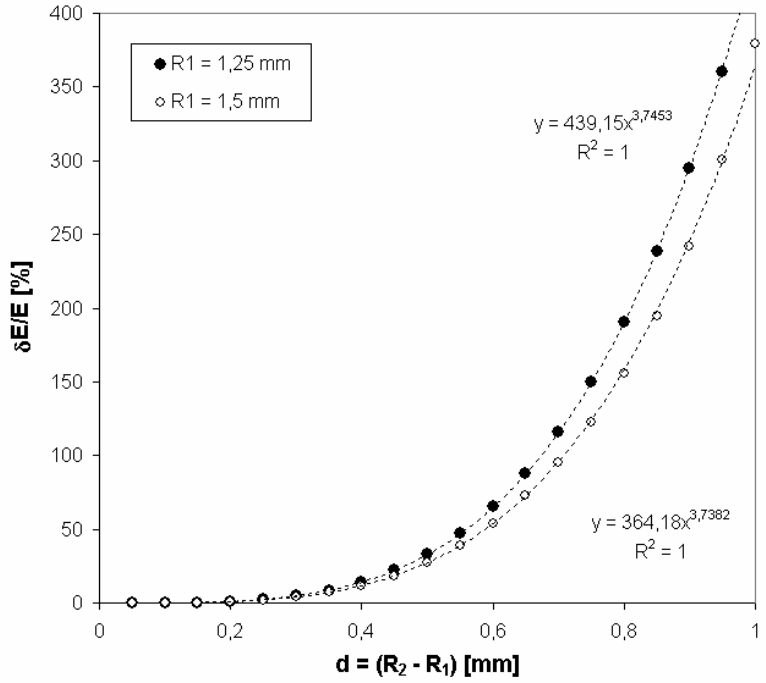

Fig. 27. Maximal distortion of the electric field as a function of the inter-electrode gap d (the filling gas is Argon at a pressure of 1 bar, R_2 = 1.75 mm, h = 1 cm, ΔV = 200 V, $\tau_f = 10^9$ f/s).

Figures 25, 26 and 27 show respectively that

- $(\delta E/E)_{max}$ varies in $1/\Delta V^2$.
- $(\delta E/E)_{max}$ varies in P^2. This result, whose simplicity was unexpected, is mainly due to the quasi-linear dependences in P of N, $1/\mu_e$ and $1/\mu_a$.
- $(\delta E/E)_{max}$ varies like $d^{15/4}$ at fixed R_1 radius for $d \leq 1$ mm. This dependence shows us that a reduction of a factor 2 on the gap d involves a reduction of a factor 13 on the space charges. It confirms the results shown in figures 23 and 24.

Consequently, using (3.16) expression, we can write

$$\left(\frac{\delta E}{E}\right)_{\max} = \frac{\delta E}{E}(r = R_2) \approx K(R_1)\frac{P^2 \tau_f d^{15/4}}{\Delta V^2}, \quad (3.17)$$

where the factor K is deduced from figures 23 and 24. We obtain $K = 3.1\ 10^7$ V^2.s.bar^{-2}.m$^{-15/4}$ for R_1 = 1.25 mm and $K = 2.7\ 10^7$ V^2.s.bar^{-2}.m$^{-15/4}$ for R_1 = 1.5 mm.
We are now able to calculate the maximum fission rate that should not be exceeded in order to avoid space charge perturbations. We consider that the space charge effect is negligible if

$$\left(\frac{\delta E}{E}\right)_{\max} \leq 5\,\%\,. \quad (3.18)$$

Using formula (3.17), this condition is equivalent to

$$\tau_f \leq 0{,}05 \frac{\Delta V^2}{K(R_1) P^2 d^{15/4}} . \quad (3.19)$$

For a standard CFUT-C3 class chamber, R_1 = 1.25 mm and R_2 = 1.75 mm. At P = 1 bar, we obtain thus

- $\tau_f \leq 4.\ 10^7$ f/s for ΔV = 100 V.
- $\tau_f \leq 1.5\ 10^8$ f/s for ΔV = 200 V.
- $\tau_f \leq 3.5\ 10^8$ f/s for ΔV = 300 V.

For a CFUT-C6 class chamber, R_1 = 1.5 mm, R_2 = 1.75 mm and we have at P = 1 bar

- $\tau_f \leq 6.2\ 10^8$ f/s for ΔV = 100 V.
- $\tau_f \leq 2.5\ 10^9$ f/s for ΔV = 200 V.
- $\tau_f \leq 5.6\ 10^9$ f/s for ΔV = 300 V.

Consequently, operating fission chambers with reduced gaps is an excellent mean to avoid space charge perturbations.

3. 3. Simplified calculations of calibration curves

When the inter-electrode gap is small compared to R_2, we can model the operation of a fission chamber with a system of equations in plane geometry. If we neglect the diffusion processes and the space charges phenomena, this system can be written

$$\begin{cases} -\dfrac{\partial}{\partial r} n_e v_e = \langle N \rangle - k n_e n_a + \alpha n_e v_e \\ \dfrac{\partial}{\partial r} n_a v_a = \langle N \rangle - k n_e n_a + \alpha n_e v_e \\ E = \dfrac{\Delta V}{R_2 - R_1} \\ n_e(R_2) = 0, n_a(R_1) = 0 \end{cases} . \quad (3.20)$$

The saturation current obtained with this approximation is given by

$$I_{sat} = e \langle S.N \rangle (R_2 - R_1) . \quad (3.21)$$

The *S.N* factor is averaged over the inter-electrode volume and we have

$$\langle S.N \rangle = \frac{1}{(R_2 - R_1)} \int_{r=R_1}^{R_2} S(r) N(r) dr = \frac{2\pi h}{(R_2 - R_1)} \int_{r=R_1}^{R_2} r N(r) dr . \quad (3.22)$$

Thus, it can be checked that the saturation current obtained with (3.21) approximation is equal to the exact expression (3.2). The (3.20) system can be solved analytically and we obtain

$$n_e(r) = \frac{C_1 \mu_a E}{2k} - \frac{Y}{2\mu_e k} \tan\left(\frac{Y(r + C_2)}{2\mu_e \mu_a E} \right), \quad (3.23)$$

with $Y = \sqrt{4\mu_a \mu_e N k - C_1^2 \mu_e^2 \mu_a^2 E^2}$.

C_1 and C_2 are two functions of E that obey the following system

$$\begin{cases} C_1 = -R_2 + \dfrac{2\mu_a \mu_e E}{Y} \arctan\left(\dfrac{\mu_a \mu_e E C_1}{Y} \right) \\ C_2 = -R_1 - \dfrac{2\mu_a \mu_e E}{Y} \arctan\left(\dfrac{\mu_a \mu_e E}{Y} (C_1 + 2\alpha(E)) \right) \end{cases} . \quad (3.24)$$

The (3.23) equation then enables us to calculate the current I delivered by the chamber according to the voltage ΔV applied to electrodes

$$I = \frac{2\pi h e R_1 \Delta V}{R_2 - R_1} \mu_e n_e(r = R_1) , \quad (3.25)$$

For R_1 = 1.25 mm, R_2 = 1.75 mm, h = 1 cm, z_{min} = -1.045 cm, z_{max} = 0.71 cm, k = 5.0 10^{-11} $m^3.s^{-1}$, P = 1 bar, X_0 = 2.10^8 pairs.m^{-1} and τ_f = 1.5 10^9 f/s, we obtain for instance the calibration curve $I = f(\Delta V)$ drawn on figure 28.

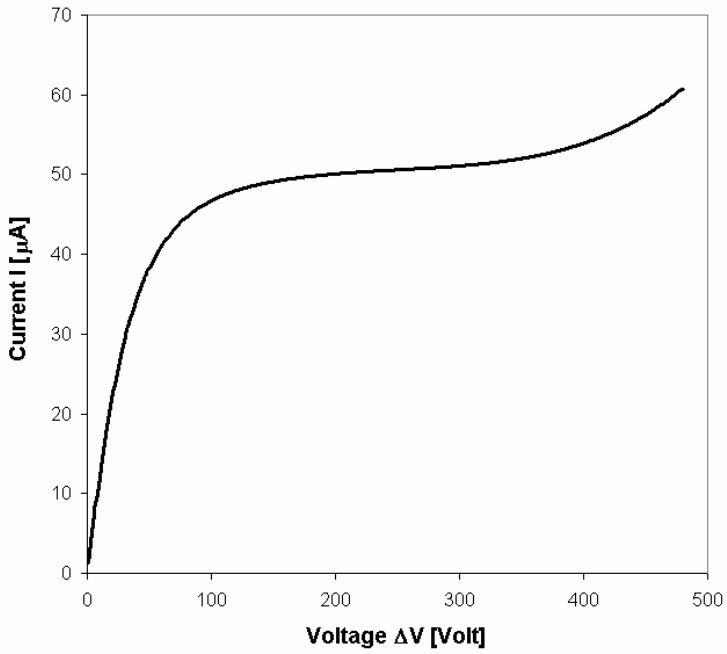

Fig. 28. Calibration curve calculated with (3.20) system. The filling gas is Argon. α is evaluated using Townsend formula.

The mobilities $\mu_e(E)$ and $\mu_a(E)$ are given by (2.51) and (2.52) expressions. The coefficient $\alpha(E)$ is given by the (2.35) Townsend formula with Zastawny coefficients [11]

$$\begin{cases} A = 2.011\ 10^5 \times P_{[\text{bar}]} \\ B = -54.7\ 10^5 \times P_{[\text{bar}]} \end{cases} . \quad (3.26)$$

This formula is simplistic and does not reproduce precisely the experimental data for weak electric field. As a consequence, we expect a poor quality description of the beginning of the avalanche. Nevertheless, we notice on figure 28 that the shape of the calibration curves is correctly reproduced by the model, with a clear saturation zone framed by the recombination mode on the left and the avalanche mode on the right. With (3.23) and (3.25) expressions, we can now study the deformation of a calibration curve according to parameters such as the gas pressure, the fission rate or the inter-electrode gap.

3. 3. 1. Evolution of the shape of a calibration curve with the recombination coefficient *k*

When the coefficient *k* decreases, we observe on figure 29 an increase in the size and quality of the saturation plateau.

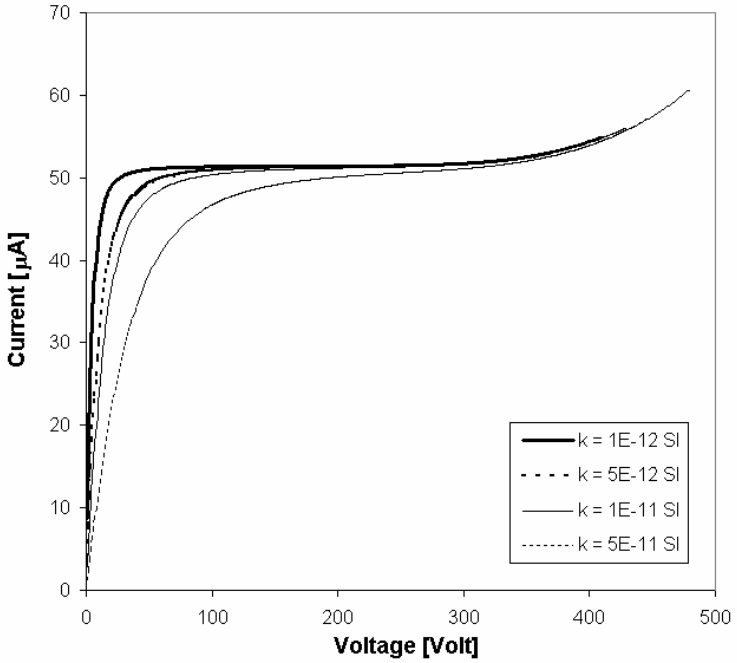

Fig. 29. Theoretical calibration curves for various coefficients *k* (the filling gas is Argon at a pressure of 1 bar, R_1 = 1.25 mm, R_2 = 1.75 mm, $\tau_f = 1.5\ 10^9$ f/s, $X_0 = 2.10^8$ pairs.m^{-1}. α is evaluated using Townsend formula).

On figures 30 and 31, we have plotted the evolution of V_{min}, V_0, V_{max} and I_0 as a function of the recombination coefficient *k*. V_0 is the voltage obtained at the inflection point of the calibration curve and I_0 the corresponding current. V_0 and I_0 are respectively called the "operating point" and "operating current". V_{min} and V_{max} are the voltages at the first and last point of the saturation plateau, respectively. They are defined for $I_{min} = 0.98\ I_0$ and $I_{max} = 1.02\ I_0$.

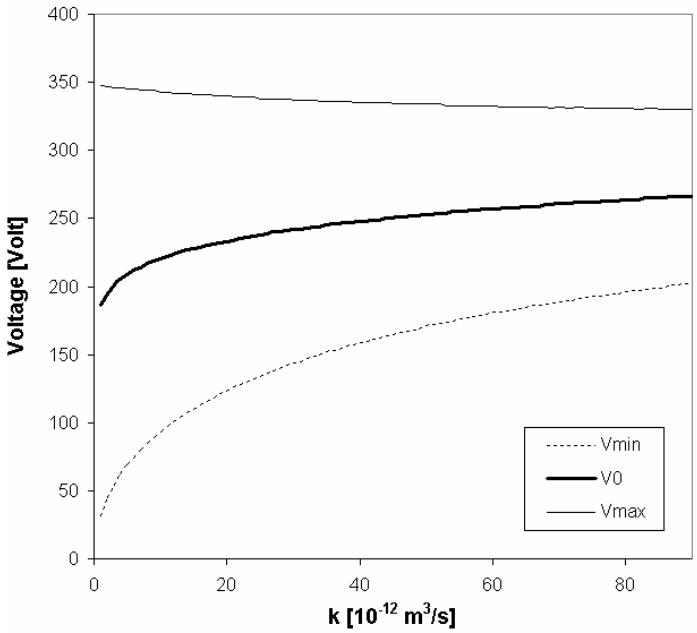

Fig. 30. Evolution of V_{min}, V_0 and V_{max} with coefficient k (the filling gas is Argon at a pressure of 1 bar, R_1 = 1.25 mm, R_2 = 1.75 mm, τ_f = 1.5 10^9 f/s, X_0 = 2.10^8 pairs.m^{-1}. α is evaluated using Townsend formula).

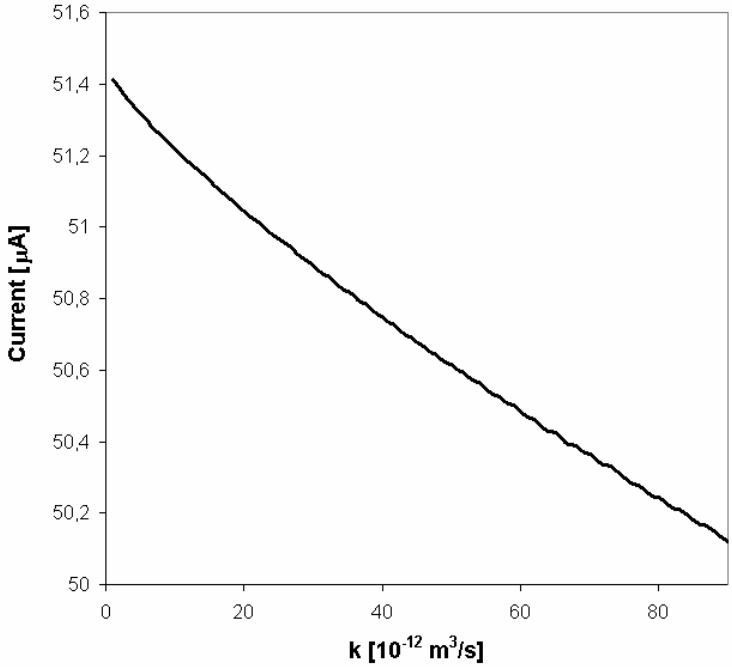

Fig. 31. Evolution of I_0 with coefficient k (the filling gas is Argon at a pressure of 1 bar, R_1 = 1.25 mm, R_2 = 1.75 mm, τ_f = 1.5 10^9 f/s, X_0 = 2.10^8 pairs.m^{-1}. α is evaluated using Townsend formula).

First, we notice that the V_{max} voltage and the I_0 current are almost independent of k on two orders of magnitude. This result is not surprising, as the recombination processes are negligible at saturation (see section 2.5 or 3.1). Secondly, when the coefficient k increases, the size of the saturation plateau, given by the difference between V_{max} and V_{min}, is reduced. Indeed, when k becomes important, the recombination processes remain non-negligible even at high voltages and the transition with the saturation mode is consequently delayed.

3. 3. 2. Evolution of the shape of a calibration curve with the fission rate

As shown on figures 32 and 33, when the fission rate increases, the saturation plateau gradually disappears and the transition between the recombination and the avalanche modes is less and less visible. The saturation plateau is progressively replaced by a mixing of recombination and secondary charge production. This behaviour is observed experimentally as already mentioned in figure 15.

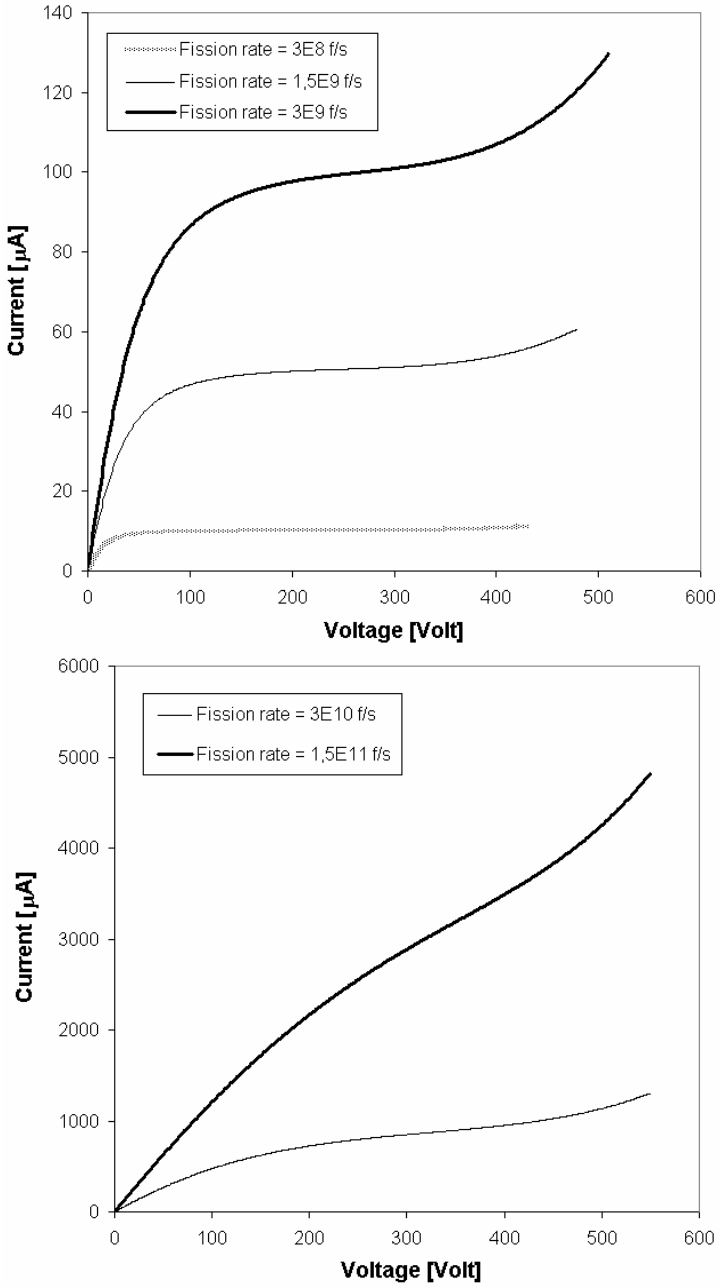

Fig. 32a and 32b. Progressive deformation of the calibration curves at high fission rates (the filling gas is Argon at a pressure of 1 bar, R_1 = 1.25 mm, R_2 = 1.75 mm, k = 5 10^{-11} m^3/s, X_0 = 2.10^8 $pairs.m^{-1}$. α is evaluated using Townsend formula).

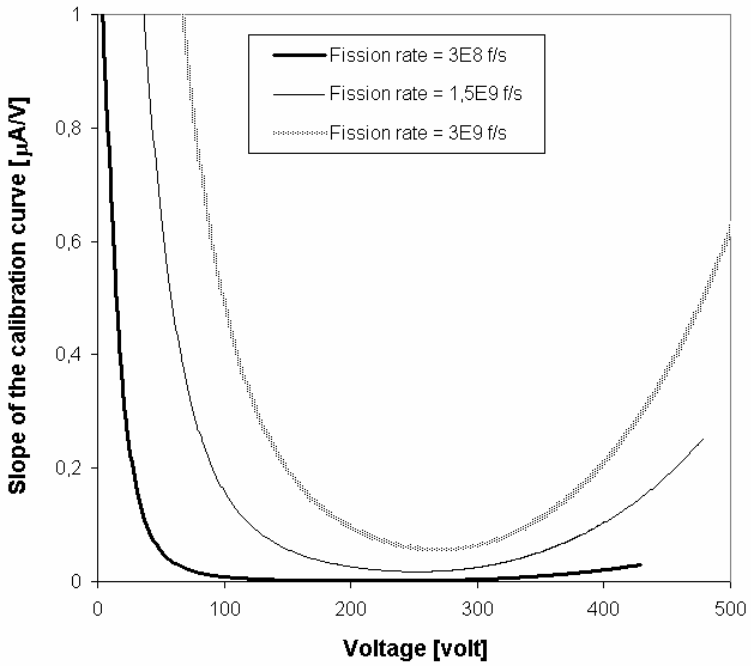

Fig. 33. Derivatives of the calibration curves for different fission rates (the filling gas is Argon at a pressure of 1 bar, R_1 = 1.25 mm, R_2 = 1.75 mm, k = 5 10^{-11} m^3/s, X_0 = 2.10^8 pairs.m^{-1}. α is evaluated using Townsend formula).

In addition, we notice on figure 34 that the operating current I_0 does not vary any more linearly with τ_f at high fission rates. This major perturbation is primarily due to the reinforcement of the recombination term kn_en_a, the charge densities increasing with τ_f. Nevertheless, a reduction of the inter-electrode volume must induce a decrease in the number of charges present in the filling gas. As a consequence, we expect that the deviation from the standard linear law will be reduced when the inter-electrode gap d decreases. This conclusion is verified on figure 35.

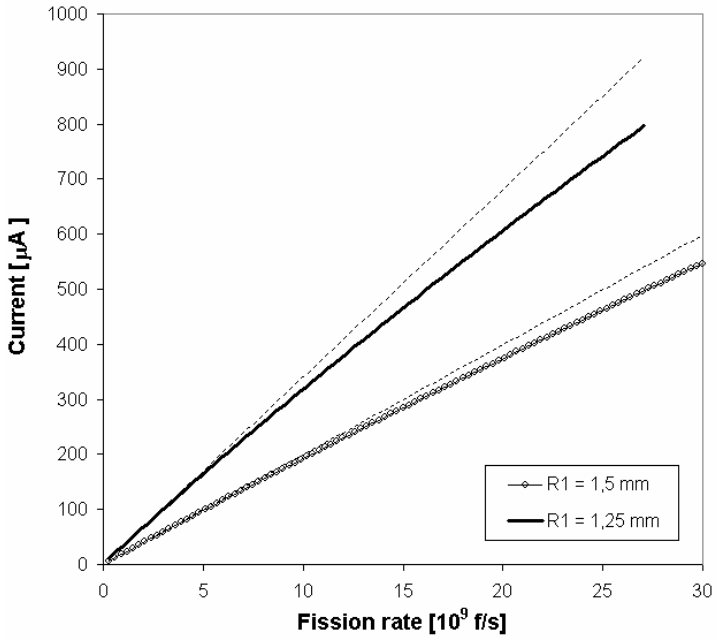

Fig. 34. Evolution of the operating current I_0 with the fission rate τ_f for two anode radiuses R_1 (the filling gas is Argon at a pressure of 1 bar, R_2 = 1.75 mm, k = 5. 10^{-11} m^3/s, X_0 = 2.10^8 pairs.m^{-1}. α is evaluated using Townsend formula).

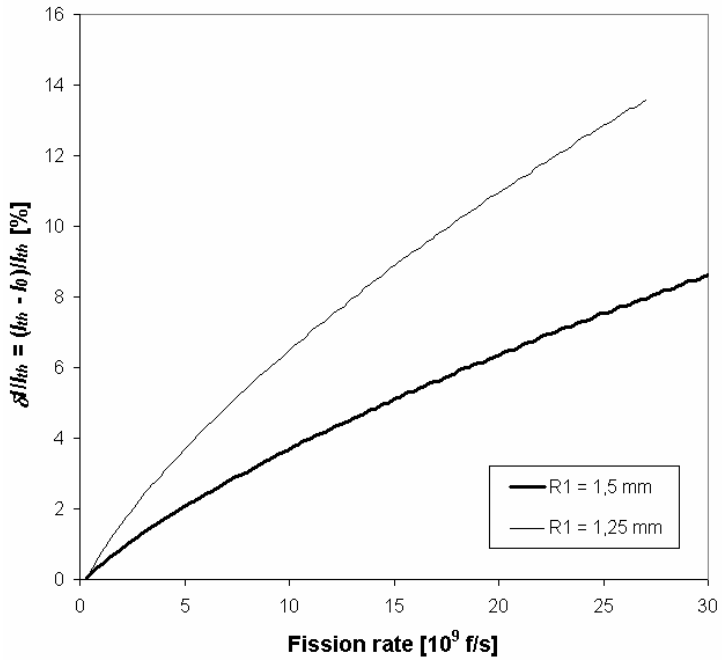

Fig. 35. Deviation in percentage from the standard linear law as a function of the fission rate. I_{th} would have been the current expected if the linear law was true (the filling gas is Argon at a pressure of 1 bar, R_2 = 1.75 mm, k = 5. 10^{-11} m^3/s, X_0 = 2.10^8 pairs.m^{-1}. α is evaluated using Townsend formula).

3. 3. 3. Evolution of the shape of a calibration curve with the gas pressure

When the filling gas pressure P increases, the electric charges move slower and the number of secondary ionizations is consequently reduced. To achieve avalanche, it is necessary to transmit more kinetic energy to electrons. An increase in P will thus induce a shift of avalanche towards higher voltages, as illustrated on figure 36.

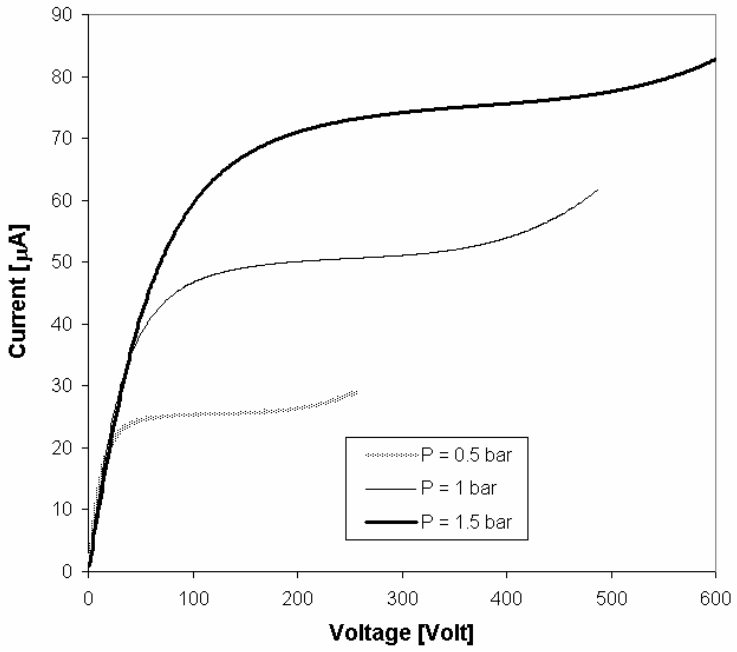

Fig. 36. Theoretical calibration curves for various gas pressures P (the filling gas is Argon, R_1 = 1.25 mm, R_2 = 1.75 mm, τ_f = 1.5 10^9 f/s, $X_0 = 2.10^8 \times P_{[bar]}$ pairs.m^{-1}. α is evaluated using Townsend formula).

The density N of electron-ion pairs created per second by the fission products increases linearly with the pressure P (via the X_0 coefficient). Moreover, the I_{sat} current is independent of the mobilities and of the first ionization coefficient. Consequently, as we can notice on figure 37, I_0 is a quasi-linear function of P for pressures close to the atmosphere.

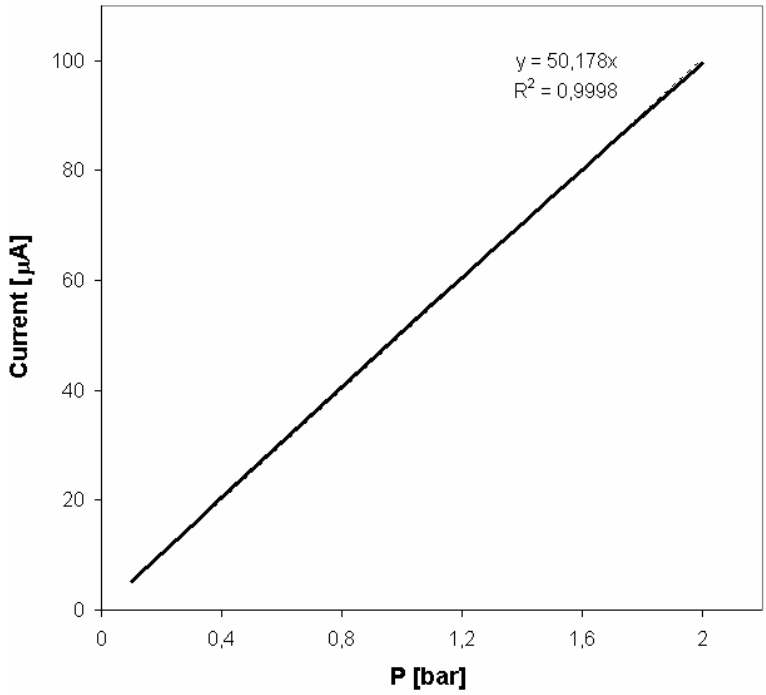

Fig. 37. Evolution of I_0 with the pressure P (the filling gas is Argon, R_1 = 1.25 mm, R_2 = 1.75 mm, τ_f = 1.5 10^9 f/s, $X_0 = 2.10^8 \times P_{[bar]}$ pairs.m^{-1}. α is evaluated using Townsend formula).

Starting from now, we will vary the pressure P while adapting the fission rate τ_f in order to maintain the saturation current I_{sat} constant. In agreement with (3.9) equation, fixing I_{sat} is equivalent to fix the product $P \times \tau_f$.

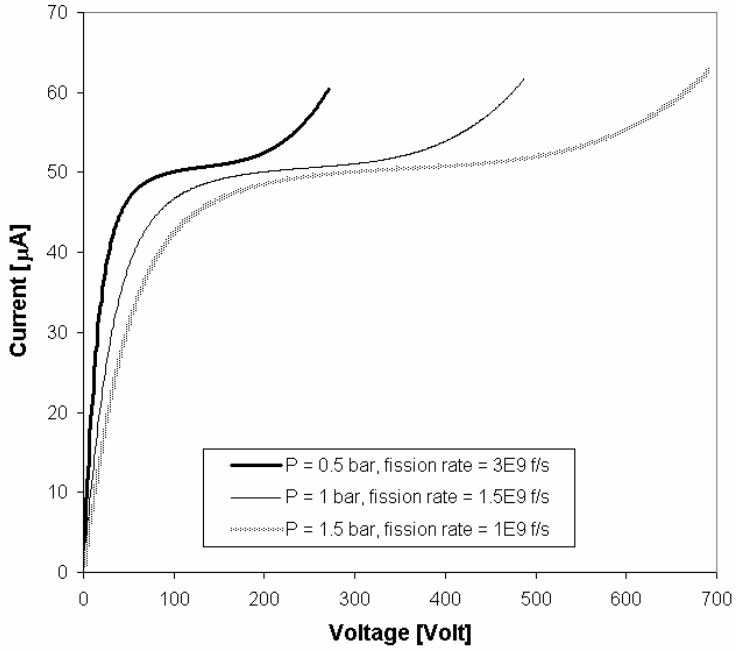

Fig. 38. Theoretical calibration curves for various gas pressures P. The fission rate is adjusted in order to maintain the saturation current constant (the filling gas is Argon, R_1 = 1.25 mm, R_2 = 1.75 mm, $X_0 = 2.10^8 \times P_{[bar]}$ pairs.m^{-1}. α is evaluated using Townsend formula).

We notice then on figure 38 that an increase in P induces a dilation of the calibration curves. In particular, the size of the saturation mode is increased (see figure 39). As a consequence, working at high pressures facilitates the measurement of the saturation current, and thus the experimental determination of the fission rate. But we have to remember that the space charges perturbations also increase with the pressure as P^2 (see chapter 3.2).

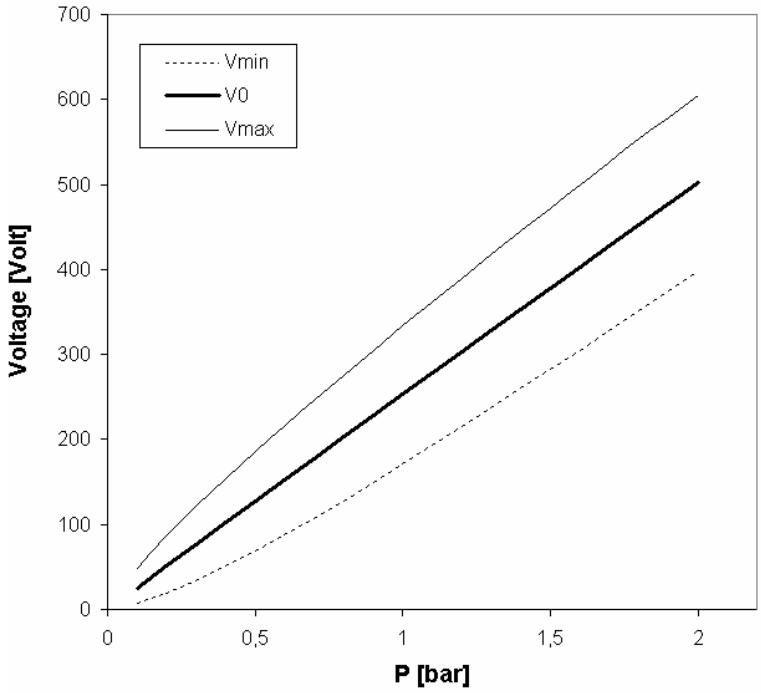

Fig. 39. Evolution of V_{min}, V_0 and V_{max} with the pressure P (the filling gas is Argon, R_1 = 1.25 mm, R_2 = 1.75 mm, $\tau_f = 1.5\ 10^9$ f/s, $X_0 = 2.10^8 \times P_{[bar]}$ pairs.m^{-1}. α is evaluated using Townsend formula).

3. 3. 4. Evolution of the shape of a calibration curve with R_1, the anode radius

At fixed cathode radius, an increase in R_1 induces a reinforcement of the electric field E, in accordance with (2.48) expression. The charge velocities will consequently grow and electrons will induce earlier secondary ionizations. Thus, the avalanche mode will start at lower voltages, as illustrated on figure 40. We notice however that this drawback is compensated by an increase in quality of the saturation plateau. Indeed, its slope progressively decreases when the inter-electrode gap d is reduced, allowing a more precise determination of the saturation current.

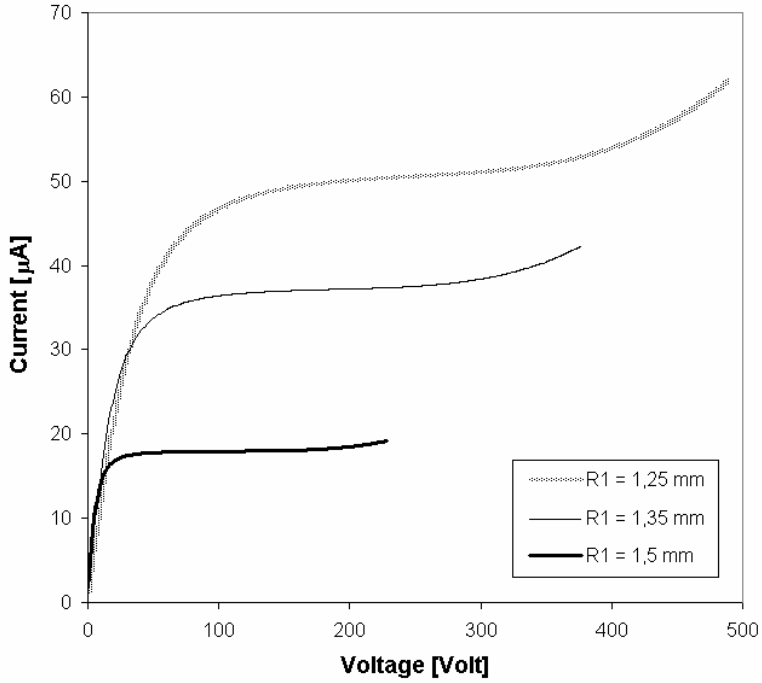

Fig. 40. Theoretical calibration curves for various anode radiuses R_1 (the filling gas is Argon at a pressure of 1 bar, R_2 = 1.75 mm, τ_f = 1.5 10^9 f/s, X_0 = 2.10^8 pairs.m^{-1}. α is evaluated using Townsend formula).

The operating current I_0 remains close to I_{sat} for common fission rates (inferior to 5.10^9 f/s for a CFUT-C3 chamber). Consequently, its sensitivity to R_1 and R_2 radii is conform to the results obtained in section 3.1.

3. 4. Calculation of the maximum voltage that should not be exceeded to avoid avalanche

In this section, we will evaluate for various pure and mixed gases the maximum voltage V_m that should not be exceeded to avoid avalanche. At the end of saturation, i.e. at the beginning of avalanche, the recombination processes are negligible. Consequently, the (3.20) system becomes

$$\begin{cases} -\dfrac{\partial}{\partial r} n_e v_e = \langle N \rangle + \alpha n_e v_e \\ \dfrac{\partial}{\partial r} n_a v_a = \langle N \rangle + \alpha n_e v_e \\ E = \dfrac{\Delta V}{R_2 - R_1} \\ n_e(R_2) = 0, n_a(R_1) = 0 \end{cases} . \quad (3.27)$$

We thus obtain

$$n_e(r) = \frac{\langle N \rangle}{\alpha(E)\mu_e(E)E}\left[e^{(R_2 - r)\alpha(E)} - 1\right], \quad (3.28)$$

and the output current I is given by

$$I = 2\pi he R_1 \frac{\langle N \rangle}{\alpha(E)} \left[e^{(R_2 - R_1)\alpha(E)} - 1 \right]. \quad (3.29)$$

To estimate V_m, we assume the condition

$$I(V_m) = 1.05\, I_{sat}, \quad (3.30)$$

This condition results in the following equation on E_m

$$\frac{e^{(R_2 - R_1)\alpha(E_m)} - 1}{\alpha(E_m)} = 1.05(R_2 - R_1). \quad (3.31)$$

This equality can be solved and leads to a condition on the first ionization coefficient α

$$\alpha(E_m) \approx \frac{0.098}{R_2 - R_1}. \quad (3.32)$$

For R_1 = 1.25 mm and R_2 = 1.75 mm, we have

$$\alpha(E_m) \approx 193.6\ \mathrm{m}^{-1}. \quad (3.33)$$

Using BOLSIG simulations presented figure 9, we have solved (3.33) equation for several gases. Results are presented in table 3.

Gas	E_m **[10^6 V.m^{-1}]**
Helium	0.289
Neon	0.289
Argon	0.502
Ar + 1 ‰ Xe	0.464
Ar + 1 % Xe	0.319

Tab. 3. Electric fields at the beginning of avalanche in a standard CFUT-C3 chamber for various gases.

With the (3.27) expression of the electric field, we finally obtain

Gas	V_m **[Volt]**
Helium	140
Neon	140
Argon	250
Ar + 1 ‰ Xe	230
Ar + 1 % Xe	160

Tab. 4. Voltage at the beginning of avalanche in a standard CFUT-C3 chamber for various gases

First, we observe on table 4 that a Neon or Helium chamber cannot work at high voltages, as avalanche appears too early. Secondly, we notice that the addition of contaminants with low ionization potentials involves a shift of avalanche towards lower voltages, as the secondary

ionization processes are facilitated. In particular, a Xenon contamination can have catastrophic consequences on the size of the saturation plateau. It is thus important to remember that this gas is one of the most abundant fission products of ^{235}U. For instance, with a 4 µg ^{235}U deposit in a 10^{15} $n.cm^{-2}.s^{-1}$ thermal neutron flux, the Xenon contamination of Argon can reach, after 40 days of irradiation, about 0.1 % in a standard CFUT-C3 chamber at a pressure of one bar. The Xenon effect is illustrated on the experimental calibration curves presented in figure 41, where we observe a shift of avalanche towards lower voltages in the course of irradiation

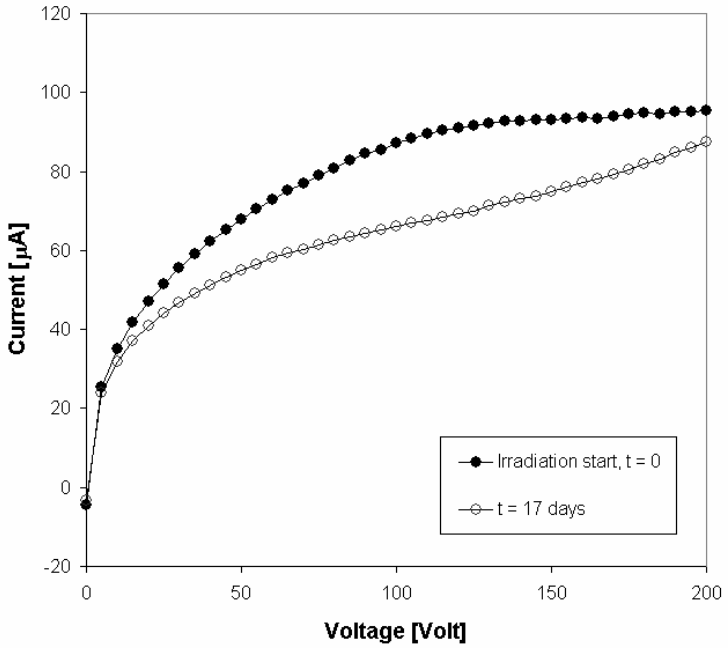

Fig. 41. Evolution of the shapes of experimental calibration curves during irradiation at ILL/Grenoble High-Flux Reactor in a 10^{15} $n.cm^{-2}.s^{-1}$ thermal neutron flux (CFUT-C3 chamber with a 98.5 % pure ^{235}U deposit).

4. Conclusion

In this article, we have proposed an overview of the physical processes that take place inside fission chambers working in current mode. We have also developed an analytical model allowing the calculation of their characteristic responses according to parameters such as the gas pressure or the fission rate. The shapes of these characteristic curves have been correctly reproduced and their evolution corresponds to the experience feedback accumulated during 5 years at ILL\Grenoble High Flux Reactor. The calculation of the electron-ion pairs density created in the filling gas by the fission products was carried out. As a consequence, the prediction of the current delivered at saturation was achieved with precision. In addition, the space charge perturbations have been quantified and the calculation of the maximum voltage that should not be exceeded to avoid avalanche has been conducted. We predict in particular a shift of avalanche towards lower voltages when contaminants such as Xenon (a fission product of Uranium 235) are present in Argon gas. This perturbation is verified during experiments and complicates notably the post-irradiation analysis. Finally, we have noticed on several occasions that a reduction of the inter-electrode gap facilitates the measurements in high neutron fluxes while limiting the perturbations usually associated with high fission rates (space charges perturbations, deformation of the curves, disappearance of the plateau, etc.).

The theoretical developments presented throughout this article will be completed by a numerical study and a computer code, currently under development.

References

[1] S. Chabod et al, Proceedings of AccApp05, Aug 29 – Sept. 1 2005, Venice, Italy, NIM A in press (2006).
[2] M. Fadil et al, NIM A 476 (2002) 313-317.
[3] M. Salvatores et al, *The MEGAPIE Initiative*, Report MPO-1-GB-6/0_GB, Paul Scherrer Institute, Zurich (1999).
[4] G. Fioni et al, Nucl. Phys. A693 (2001) 546.
[5] F. Marie et al, ND2004, Proceedings of International Conference on Nuclear Data for Science and Technology, Sept 26 – Oct 01 2004, Santa Fe, USA.
[6] A. Letourneau et al, ND2004, Proceedings of International Conference on Nuclear Data for Science and Technology, Sept 26 – Oct 01 2004, Santa Fe, USA.
[7] O. Poujade, A. Lebrun, NIM A 433 673-682 (1999).
[8] Available in freeware at www.srim.org.
[9] ICRU report, *Average energy required to produce an ion pair* (1979).
[10] St. Behle et al, Plasma Sources Sci. Technol. 9 57-67 (2000).
[11] A. Zastawny, NIM A 385 239-242 (1997).
[12] Available in freeware at www.siglo-kinema.com.
[13] C S. Lakshminarasimha et al, J. Phys. D, Appl. Phys. Vol. 10, 313-321 (1997).
[14] L. Onsager, Phys. Rev. Vol. 54 554-557 (1938).
[15] I. S. Grigoriev, E. Z. Meilikhov, *Handbook of Physical Quantities* (CRC Press, Inc.) (1997).
[16] K. Shinsaka et al, J. Chem. Phys. 88 (12) (1988).
[17] S. Flügge, G. Francis, Phys. Handbook, Vol 22, *Gas Discharges II* (Springer-Verlag, Berlin) (1956).
[18] M. A. Biondi, Phys. Rev. 129 3 1181-1188 (1963).
[19] Atomic Data and Nuclear Data Tables n° 17, *Transport properties of gaseous ions over a wide energy range* (1976).
[20] J. A. Hornbeck, Phys. Rev. Vol. 84, n° 4, 615-620 (1951).
[21] S. Robertson et al, Phys. Rev. E 67 046405 (2003).